

Original Research

Electroosmotic and Gyrotactic Microorganisms Effects on MHD $\text{Al}_2\text{O}_3\text{-Cu}$ /Blood Hybrid Nanofluid Flow through Multi-Stenosed Bifurcated Artery

Umesh Khanduri¹, Bhupendra Kumar Sharma¹, Bandar Almohsen²,
Muhammad Mubashir Bhatti^{3,4,*}¹Department of Mathematics, Birla Institute of Technology and Science, 333031 Pilani, Rajasthan, India²Department of Mathematics, College of Science, King Saud University, 11451 Riyadh, Saudi Arabia³College of Mathematics and Systems Science, Shandong University of Science and Technology, 266590 Qingdao, Shandong, China⁴Material Science Innovation and Modelling (MaSIM) Research Focus Area, North-West University (Mafikeng Campus), Private Bag X2046, Mmabatho 2735, South Africa*Correspondence: mmbhatti@sdust.edu.cn; muhammad09@shu.edu.cn; mubashirme@hotmail.com (M.M. Bhatti)

Academic Editor: Cezar Comanescu

Submitted: 9 November 2023 Revised: 18 December 2023 Accepted: 3 January 2024 Published: 19 March 2024

Abstract

Background: The purpose of this study is to investigate the electroosmotic flow of a hybrid nanofluid ($\text{Al}_2\text{O}_3\text{-Cu}$ /Blood) with gyrotactic microorganisms through a bifurcated artery with mild stenosis in both parent and daughter arteries. The flow is subjected to a uniform magnetic field, viscous dissipation, and a heat source. **Methods:** The governing equations undergo the non-dimensional transformation and coordinate conversion to regularize irregular boundaries, then solve the resulting system using the Crank-Nicolson method. **Results:** In both sections of the bifurcated artery (parent and daughter artery), the wall shear stress (WSS) profile decreases with increasing stenotic depth. Nusselt profile increases with an increase in the heat source parameter. **Conclusions:** The present endeavour can be beneficial for designing better biomedical devices and gaining insight into the hemodynamic flow for therapeutic applications in the biomedical sciences.

Keywords: bifurcated artery; Joule heating; stenosis; MHD flow; hybrid nanoparticles

1. Introduction

Numerous studies have been conducted to analyse the hemodynamic characteristics of blood flow through channels, pipes and tubes to understand the pathological mechanism that arises in the stenotic artery. The study provides researchers with insights into hemodynamic flow and facilitates the development of more effective preventative treatments for diseases. Arteriosclerosis, also known as stenosis, is a pathological phenomenon characterised by the accumulation of various substances such as lipids, proteins, fatty compounds, calcium, and other cellular debris along the walls of arteries. This accumulation can result in partial occlusion or complete blockage of the affected blood vessel. A mathematical model was developed by Young [1] to investigate the Newtonian flow within a time-dependent stenosed tube. The study's findings indicate that the occurrence of stenosis within the artery disrupts the physiological processes of the cardiovascular system, ultimately resulting in severe pathological consequences. The study by Akbar *et al.* [2] delved into the intricacies of the non-Newtonian fluid model, specifically concerning blood flow within a tapered stenosed artery. The authors approached this investigation by considering blood as a Jeffery fluid. Shit and Roy [3] conducted a study on micropolar fluid to investigate the impact of induced magnetic fields on blood flow through the constricted artery. The study's findings indicate a positive correlation between the Hartman number and stenosis height with an enhancement in microcirculation. Tripathi and Sharma [4] developed a mathematical model to analyse the two-phase hemodynamic flow through a stenosed artery, incorporating chemical reactions and radiation effects. The study illustrated a reduction in blood velocity adjacent to the arterial wall, as evidenced by the distortion of the velocity contour downstream and the shift of the tapering bolus towards the arterial wall. The study conducted by Khanduri and Sharma [5,6] pertained to the examination of the impact of Hall effects on the flow of magnetohydrodynamic (MHD) fluid through a stenosed artery that has been affected by thrombosis. The study's findings indicate a decline in the wall shear stress (WSS) profile as the Hartman number and stenotic depth increase. This phenomenon is caused by reduced blood flow near the arterial walls.

The study revealed that atherosclerotic plaque, which obstructs blood flow in arteries, tends to manifest in regions of complex geometry, such as those proximal to bifurcations, junctions, or areas of high curvature. The presence of arterial curvature and variations in the size of the cross-section both had a role in the preferred localization of the plaque at the arterial walls. Tan *et al.* [7] explored the blood flow through the bifurcated artery under the gravity effect and irregular stenosis at the



parent artery. Srinivasacharya and Rao [8] have designed a mathematical model to investigate the hemodynamic behaviour of blood flow containing copper nanoparticles within a constricted bifurcated artery. The study's findings indicate a notable alteration in the flow rate and impedance near the apex. This phenomenon is attributed to the occurrence of backflow at the junction and the presence of secondary flow in the region proximal to the apex. Moreover, the researchers [9] proceeded with their investigation by examining the behaviour of a couple's stress fluid within a bifurcated artery. Shahzadi [10] conducted a theoretical analysis to explore the bio-nanofluid containing copper nanoparticles as a therapeutic agent in the bifurcated artery with compliant walls. The non-Newtonian Casson fluid was investigated by Shahzad *et al.* [11] in the context of a bifurcated channel featuring stenosis and elastic walls.

The study of blood rheology is affected by the application of external magnetic and electric fields, resulting in the reduction of the fluid flow, and such type of flow is commonly referred to as electro-magneto hydrodynamics (EMHD) flow. Kolin [12] introduced the concept of MHD in his medical research. The experiments demonstrate that applying a transverse magnetic field to an electrical field decelerates fluid motion. The empirical finding indicated a decrease of 30% in the volumetric blood flux within the duct subject to a high magnetic field of 10 Tesla. Ahmed and Nadeem [13] have constructed a mathematical model encompassing six distinct types of stenosis and have subsequently conducted an investigation on the effect of MHD and hybrid nanoparticles on micropolar fluid. The study revealed an increase in velocity and WSS with an enhancement in nanoparticle concentrations, while an inverse trend was observed for the impedance profile. The MHD fluid flow in an artery was explored numerically by Joshua *et al.* [14] by employing a non-Newtonian Cross-rheological model. The researchers have considered the presence of multiple stenoses along the arterial walls and have conducted a comprehensive investigation by varying the magnetic parameter, Reynolds number, and stenosis height throughout the entire length of the artery. Kumar *et al.* [15] analysed MHD fluid flow in a bifurcated artery with permeability, considering the effect of heat source and chemical reaction. The EMHD flow of Au-blood through the inclined constricted artery under periodic body acceleration was investigated by Manchi and Ponalagusamy [16]. The researchers also emphasised the shape of nanoparticles and concluded that the spherical nanoparticles exhibit a greater heat flux at the arterial walls than other nanoparticle shapes. Sharma *et al.* [17] formulated the MHD two-phase blood flow model by considering the variable viscosity in a curved artery. The study's findings suggest that atherosclerosis formation positively correlates with curvature and permeability, whereas the heat source parameter reduces the risk of atherosclerosis formation. The study conducted by Mishra *et al.* [18] delved into the characteristics of magnetohydrodynamic (MHD) nanofluid as it flows through a constricted artery while considering the Soret and Dufour effects. The optimisation of heat transfer in nanofluid blood flow through the stenosed artery was discussed by Sharma *et al.* [19]. The authors examined the hematocrit-dependent viscosity model and demonstrated that increased hematocrit level and stenosis depth lead to reduced fluid velocity.

Electrokinetics refers to the phenomenon wherein particles are propelled in response to electrical potential differences. Electroosmosis is an electrokinetic phenomenon that arises from applying an external electric field to a charged surface. The flow of an electrically conductive fluid within the blood vessels establishes a net charge at the vessel walls. This, in turn, leads to the development of an opposite charge due to the principle of electro-neutrality within the electrical double layer in close proximity to the walls. The investigation by Mekheimer *et al.* [20] focused on analysing the impact of electroosmotic and bifurcation effects on the hemodynamic flow in a bifurcated artery with stenosis along the parent artery. Hybrid nanofluid flow through a diseased artery with aneurysmal and stenosed segments at the walls was discussed by Abdelsalam *et al.* [21]. The study's findings indicate a correlation between the nanoparticle shape factor and the fluid velocity profile. The study suggests that this information can be applied to improve drug delivery systems. Akhtar *et al.* [22] elucidated the electroosmotic modulated flow through an artery with multiple stenoses. The dependence of trapping symmetry on the symmetry of multiple stenoses and regulating fluid velocity, temperature, and velocity through electroosmosis are notable findings in this study. In their research, Akram *et al.* [23] compared the Tiwari-Das model and the modified Buongiorno model to investigate the electroosmotic nanofluid flow under peristaltic pumping. In their study, Khanduri *et al.* [24] conducted a sensitivity analysis on the MHD fluid flow through a curved artery with stenosis at the wall and thrombosis at the catheter. The WSS profile negatively correlates with the Debye-Huckel parameter and Hartmann number, whereas the impedance profile displays an opposite trend. The EMHD micropolar fluid was analysed by Manchi *et al.* [25] in the context of a bifurcated artery, considering the effects of Joule heating and body acceleration. The topic of discussion by Zaher *et al.* [26] pertained to the flow of non-Newtonian fluid with microorganisms in the presence of electroosmotic flow within the boundary layer. In non-Darcian fluid, the velocity is observed to be lower when compared to that of Darcian fluid.

Both theoretical and experimental results have underscored the significance of nanoparticles in the biomedical domain, as they have been shown to augment the efficacy of delivering diagnostic and therapeutic agents. Numerous investigations have been undertaken to examine the novel potential of nanoparticles at the molecular scale within the realm of life sciences. The successful delivery of nanoparticles into the artery is primarily determined by their physical characteristics, including shape, size, and surface absorption properties. Nanofluid is a suspension of nanoparticles in a base fluid, whereas hybrid nanofluid is a suspension of two or more types of nanoparticles in the base fluid. Synthesis of hybrid nanofluids offers

the advantage of incorporating diverse materials' physical and thermal properties into a singular, homogeneous phase. This results in remarkable physicochemical properties in the resulting synthetic hybrid nanofluid. The hemodynamic flow through permeable walls was investigated by Ellahi *et al.* [27], employing the homotopy analysis method. The hybrid nanofluid flow through a stenosed artery was analysed by Gandhi *et al.* [28] in the presence of Joule heating and viscous dissipation. The findings of their research indicate that an increase in the Darcy number results in an enhancement of the velocity profile. This can be attributed to the lower resistance offered by the medium permeability. The researcher, Basha [29], analysed the inclined, uneven, and stenosed artery to investigate the biomagnetic blood flow of Au-Cu. The study conducted by Rishu [30] involved an investigation of the behaviour of Au-Cu hybrid nanoparticles in the context of blood flow through an artery with overlapping stenosis at the walls. The study revealed that an augmentation in the Casson fluid parameter enhances both velocity and temperature. The researchers suggest their findings may have potential applications in nano-pharmacology and biomedical sciences. Kumawat *et al.* [31] investigated the behaviour of a two-phase power-law nanofluid within a stenosed artery characterized by curvature. Their findings indicate that the presence of arterial curvature augments the likelihood of atherosclerosis deposition. In this investigation, we have opted for Al_2O_3 -Cu nanoparticles due to their exceptional anti-bacterial and anti-viral properties, offering potential applications in the biomedical domain. The chemical stability and convenient accessibility of these nanoparticles render them an ideal selection for our research.

Bioconvection refers to the phenomenon whereby the macroscopic motion of microorganisms occurs due to spatial variations in density. Microorganisms exhibit self-propulsion, whereas nanoparticles lack this capability. The phenomenon of bioconvection can be observed under conditions where the concentration of nanoparticles is relatively low. The phenomenon of bioconvection is observed due to the instability caused by spatial variation, which leads to the upward movement of microorganisms and the formation of a dense layer at the surface. This layer becomes unstable and results in the crumbling of microorganisms, further enhancing the bioconvection process. Bhatti *et al.* [32] have discussed the peristaltic motion of Jeffery nanofluid in the presence of microorganisms and a variable magnetic field. The bioconvection movement of microorganisms in a hybrid nanofluid through a porous stretching sheet was investigated by Alharbi *et al.* [33]. The study conducted by Sharma *et al.* [34] delved into the dynamics of magnetohydrodynamic (MHD) fluid flow in the presence of microorganisms over an inclined stretching sheet. Mekheimer *et al.* [35] conducted a study on the delivery of drugs via nanoparticles in the presence of hemodynamic flow within diseased organs. The study conducted by Mostapha *et al.* [36] was a theoretical investigation of the flow of peristaltic-induced nanofluid, wherein motile gyrotactic microorganisms are observed to move through an endoscope. The study considered the effects of radiation and chemical interaction while incorporating the Soret and Dufour scheme. Khan [37] applied the Homotopy Analysis Method (HAM) to explore the bioconvection phenomena in a hybrid nanofluid with gyrotactic microorganisms. Furthermore, Khan *et al.* [38] conducted a study on entropy generation analysis for the hybrid nanofluid ($\text{Ag-Al}_2\text{O}_3/\text{H}_2\text{O}$) past a semi-infinite plate. The study mentioned above indicates that no research has been conducted on the electroosmotic flow with gyrotactic microorganisms through the bifurcated artery.

In the aforementioned studies, a notable research gap becomes evident due to the need for more investigations into the behaviour of Al_2O_3 -Cu/Blood hybrid nanofluids containing gyrotactic microorganisms. Specifically, there is a lack of examination of the hybrid nanofluid flow through multi-stenosed bifurcated arteries with the electroosmotic effect. Filling this research gap is crucial for comprehensively understanding the flow characteristics, thermal characteristics, and biological interactions within such complex vascular conditions. The previously mentioned study has inspired and formed the basis for our ongoing research on the hybrid nanofluids flow in the bifurcated arteries with mild stenosis in both parent and daughter arteries. This study introduces a model that examines the blood flow behavior containing suspended nanoparticles of Al_2O_3 -Cu, in the presence of gyrotactic microorganisms and electroosmotic force. The governing equations are made non-dimensional and subsequently solved using the Crank-Nicolson scheme. The resulting outcomes are analyzed, and the effects of various parameters are clarified by plotting velocity, temperature, concentration, microorganisms, flow rate, and WSS profiles.

The novelty of the present work:

- To investigate the influence of hybrid nanofluid (Al_2O_3 -Cu/Blood) flow with gyrotactic microorganism through the stenosed bifurcated artery.
- Examine the blood flow characteristics with combined effect of Joule heating, electroosmosis, heat source and viscous dissipation.

2. Model Formulation

Consider a fully developed, unsteady, laminar, incompressible two-dimensional MHD blood flow passing through the stenosed bifurcated artery. The arteries are assumed to be straight, circular cylinders passing the centre line of the parent artery. The bifurcated artery has overlapping stenosis at the parent artery, while the irregular stenosis at the daughter arteries is shown in Fig. 1. Let's assume the cylindrical coordinate system r_1^* , θ_1^* and z_1^* to represent the material point in which z_1^* is along the centerline of the parent artery and r_1^* and θ_1^* are assumed to be radial and circumferential directions, respectively.

The flow is assumed to be antisymmetric, so all the variables are independent of θ . A uniform magnetic field denoted by $\mathbf{B} = (B_0, 0, 0)$ and an electric field denoted by $\mathbf{E} = (0, 0, E_0)$ are applied to the flow of blood, where B_0 is constant. The gravitational force acts in the downward direction and the induced magnetic field is assumed to be negligible due to low magnetic Reynold's number assumption. The potential for a flow separation zone is eliminated by incorporating curvature at the lateral junction and bifurcation's apex.

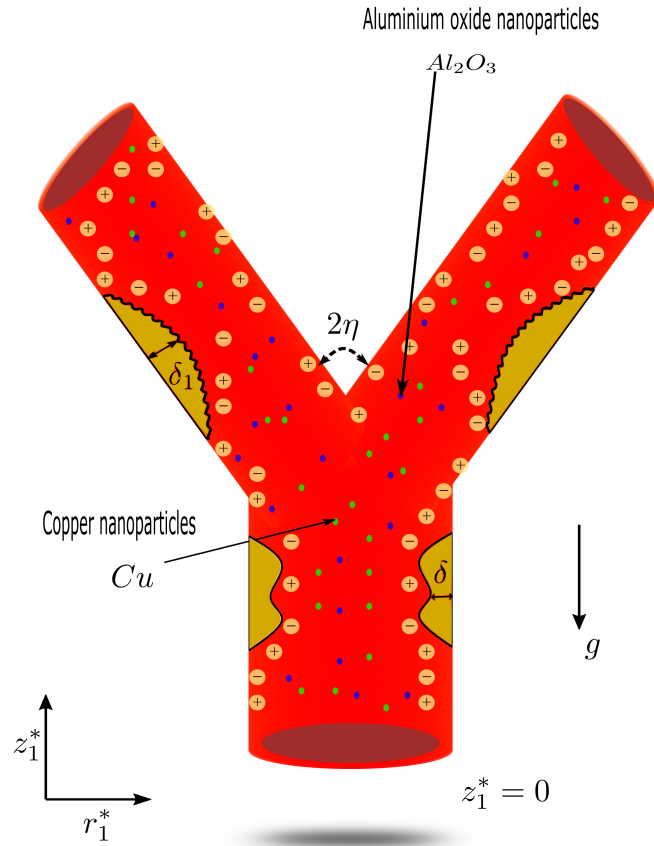


Fig. 1. Representation of bifurcated stenosed artery.

The geometry of the bifurcated artery with multi-stenosis in the parent artery and an overlapping stenosis in the daughter artery is expressed as follows [10]:

$$R_1^*(z_1^*) = \begin{cases} R_0, & 0 < z_1^* \leq d \\ R_0 - \frac{6}{5L_0^4} \delta (11(z_1^* - d)L_0^3 - 47(z_1^* - d)^2 L_0^2 + 72(z_1^* - d)^3 L_0 - 36(z_1^* - d)^4), & d < z_1^* \leq d + L_0 \\ R_0, & d + L_0 < z_1^* \leq z_1 \\ R_0 + r_1 - \sqrt{\left(r_1^2 - \frac{R_0^2}{L_0^2} (z_1^* - z_1)^2\right)} & z_1 < z_1^* \leq z_2 \\ 2r_0 \sec \eta + \frac{R_0}{L_0} \left(z_1^* - z_2\right) \tan \eta & z_2 < z_1^* \leq z_4 + 0.5L_0 \\ 2r_0 \sec \eta + \frac{R_0}{L_0} \left(z_1^* - z_2\right) \tan \eta - A^* & z_4 + 0.5L_0 < z_1^* \leq z_4 + 2.5L_0, \\ 2r_0 \sec \eta + \frac{R_0}{L_0} \left(z_1^* - z_2\right) \tan \eta, & z_4 + 2.5L_0 < z_1^* \leq z_{max}, \end{cases} \quad (1)$$

where $A^* = 2\delta_1 \left\{ \cos \left(\frac{2\pi}{L_0} \left(\frac{z_1^* - d}{4} \right) - 0.25 \right) - 0.07 \cos \left(\frac{128\pi}{L_0} \left(z_1^* - d - 0.5L_0 \right) \right) \right\} \tan(\eta)$, R_0 represents the radius of

the normal artery, L_0 is the length of the diseased segment and Kroncecker delta function is defined as:

$$\delta_{ij} = \begin{cases} 0 & \text{for } 0 \leq z_1^* \leq z_3, \\ 1 & \text{for } z_3 \leq z_1^* \leq z_{max}, \end{cases} \quad (2)$$

The inner wall is represent as:

$$R_2^*(z_1^*) = \begin{cases} 0, & 0 < z_1^* \leq z_3, \\ \sqrt{\tilde{r}_1^2 - \left(R_0 \left(\frac{z_1^* - z_3}{L_0}\right) - \tilde{r}_1\right)^2}, & z_3 < z_1^* \leq z_4, \\ \frac{R_0}{L_0}(z_1^* - z_2) \tan \eta, & z_4 < z_1^* \leq z_{max}. \end{cases} \quad (3)$$

Where, d represent location of stenosis, z_1 denotes the location of insert lateral junction, z_{max} signifies the maximum length of stenosis; The radii of curvature at the flow divider and at lateral junction is represented by:

$$\tilde{r}_1 = \frac{(z_3 - z_2)R_0 \sin \eta}{L_0(1 - \sin \eta)}, \quad r_1 = \frac{R_0 - 2r_0 \sec \eta}{\cos \eta - 1}, \quad (4)$$

The positional of the lateral junction offset, apex, and curvature offset at the inner wall are presented as follows:

$$z_2 = z_1 + r_1 \left(\frac{L_0}{R_0}\right) \sin \eta, \quad (5)$$

$$z_3 = z_2 + q_1 L_0, \quad (6)$$

$$z_4 = z_3 + \tilde{r}_1 \left(\frac{L_0}{R_0}\right) (1 - \sin \eta). \quad (7)$$

Where η is half of the bifurcation angle and value of q_1 lies between 0.1 and 0.5, z_{max} represents the finite length of the bifurcated artery.

2.1 Governing Equations

Assuming the aforementioned conditions and utilising the Boussinesq approximation, the equations dictating the flow can be expressed as follows [30]:

Continuity Equation:

$$\frac{\partial u_1^*}{\partial r_1^*} + \frac{u_1^*}{r_1^*} + \frac{\partial w_1^*}{\partial z_1^*} = 0, \quad (8)$$

Momentum Equation:

r_1^* -direction:

$$\rho_{hnf} \left[\frac{\partial u_1^*}{\partial t_1^*} + u_1^* \frac{\partial u_1^*}{\partial r_1^*} + w_1^* \frac{\partial u_1^*}{\partial z_1^*} \right] = -\frac{\partial p_1^*}{\partial r_1^*} + \frac{1}{r_1^*} \frac{\partial}{\partial r_1^*} \left[\mu_{hnf} r_1^* \frac{\partial u_1^*}{\partial r_1^*} \right] + \frac{1}{2} \frac{\partial}{\partial z_1^*} \left[\mu_{hnf} \left(\frac{\partial w_1^*}{\partial r_1^*} + \frac{\partial u_1^*}{\partial z_1^*} \right) \right] - \mu_{hnf} \frac{u_1^*}{r_1^{*2}}, \quad (9)$$

z_1^* -direction:

$$\rho_{hnf} \left[\frac{\partial w_1^*}{\partial t_1^*} + u_1^* \frac{\partial w_1^*}{\partial r_1^*} + w_1^* \frac{\partial w_1^*}{\partial z_1^*} \right] = -\frac{\partial p_1^*}{\partial z_1^*} + \frac{1}{2} \frac{1}{r_1^*} \frac{\partial}{\partial r_1^*} \left[\mu_{hnf} r_1^* \left(\frac{\partial u_1^*}{\partial z_1^*} + \frac{\partial w_1^*}{\partial r_1^*} \right) \right] + \frac{\partial}{\partial z_1^*} \left[\mu_{hnf} \frac{\partial w_1^*}{\partial z_1^*} \right] + (\rho\gamma)_{hnf} g \left[(\tilde{T}^* - \tilde{T}_1^*) + (\tilde{C}^* - \tilde{C}_1^*) - (\tilde{n}^* - \tilde{n}_1^*) \right] \cos(\eta\delta_{ij}) + G(t_1^*) + \rho_e E_0 - \sigma_{hnf} B_0^2 w_1^*, \quad (10)$$

Energy Equation:

$$(\rho C_p)_{hnf} \left[\frac{\partial \tilde{T}^*}{\partial t_1^*} + u_1^* \frac{\partial \tilde{T}^*}{\partial r_1^*} + w_1^* \frac{\partial \tilde{T}^*}{\partial z_1^*} \right] = k_{hnf} \left[\frac{\partial^2 \tilde{T}^*}{\partial r_1^{*2}} + \frac{1}{r_1^*} \frac{\partial \tilde{T}^*}{\partial r_1^*} + \frac{\partial^2 \tilde{T}^*}{\partial z_1^{*2}} \right] + \tilde{Q}_0 + \sigma_{hnf} B_0^2 w_1^{*2} + \sigma_{nf} E_0^2 + \phi^*, \quad (11)$$

where,

$$\phi^* = 2\mu_{hnf} \left[\left(\frac{\partial u_1^*}{\partial r_1^*} \right)^2 + \left(\frac{u_1^*}{r_1^*} \right)^2 + \left(\frac{\partial w_1^*}{\partial z_1^*} \right)^2 + \frac{1}{2} \left(\frac{\partial u_1^*}{\partial z_1^*} + \frac{\partial w_1^*}{\partial r_1^*} \right)^2 \right].$$

Concentration Equation:

$$\frac{\partial \tilde{C}^*}{\partial t_1^*} + u_1^* \frac{\partial \tilde{C}^*}{\partial r_1^*} + w_1^* \frac{\partial \tilde{C}^*}{\partial z_1^*} = D_b \left[\frac{\partial^2 \tilde{C}^*}{\partial r_1^{*2}} + \frac{1}{r_1^*} \frac{\partial \tilde{C}^*}{\partial r_1^*} + \frac{\partial^2 \tilde{C}^*}{\partial z_1^{*2}} \right] - R_c(\tilde{C}^* - \tilde{C}_1^*) \quad (12)$$

Microorganism Equation:

$$\frac{\partial \tilde{n}^*}{\partial t_1^*} + u_1^* \frac{\partial \tilde{n}^*}{\partial r_1^*} + w_1^* \frac{\partial \tilde{n}^*}{\partial z_1^*} + \frac{bW_c}{\tilde{C}_0^* - \tilde{C}_w^*} \left[\frac{\partial}{\partial r_1^*} \left(\tilde{n}^* \frac{\partial \tilde{C}^*}{\partial r_1^*} + \frac{\partial}{\partial z_1^*} \left(\tilde{n}^* \frac{\partial \tilde{C}^*}{\partial z_1^*} \right) \right) \right] = D_n \left[\frac{\partial^2 \tilde{n}^*}{\partial r_1^{*2}} + \frac{1}{r_1^*} \frac{\partial \tilde{n}^*}{\partial r_1^*} + \frac{\partial^2 \tilde{n}^*}{\partial z_1^{*2}} \right] \quad (13)$$

The boundary conditions are:

$$w_1^* = 0, \quad \tilde{T}^* = \tilde{T}_w^*, \quad \tilde{C}^* = \tilde{C}_w^*, \quad \tilde{n}^* = \tilde{n}_w^* \quad \text{at } r_1^* = R_1(z_1^*) \quad \text{for all } z_1^*, \quad (14)$$

$$\frac{\partial w_1^*}{\partial r_1^*} = 0, \quad \frac{\partial \tilde{T}^*}{\partial r_1^*} = 0, \quad \frac{\partial \tilde{C}^*}{\partial r_1^*} = 0, \quad \frac{\partial \tilde{n}^*}{\partial r_1^*} = 0 \quad \text{at } r_1^* = 0 \quad \text{for } 0 \leq z_1^* \leq z_3, \quad (15)$$

$$w_1^* = 0, \quad \tilde{T}^* = \tilde{T}_w^*, \quad \tilde{C}^* = \tilde{C}_w^*, \quad \tilde{n}^* = \tilde{n}_w^* \quad \text{at } r_1^* = R_2(z_1^*) \quad \text{for } z_3 \leq z_1^* \leq z_{max}. \quad (16)$$

The initial condition regarding velocity, temperature, concentration and microorganisms are considered as:

$$w_1^* = 0, \quad \tilde{T}^* = 0, \quad \tilde{C}^* = 0, \quad \tilde{n}^* = 0 \quad \text{at } t_1^* = 0. \quad (17)$$

The body acceleration and pressure gradient terms are given as;

$$G(t_1^*) = \tilde{F}_b \cos(\omega_b t_1^* + \psi) \quad (18)$$

$$-\frac{\partial p_1^*}{\partial z_1^*} = D_0 + D_1 \cos(\omega_p t_1^*) \quad (19)$$

Here, $\omega_p = 2\pi\nu_p$, ν_p is pulse frequency, \tilde{F}_b is the body acceleration term, $\omega_b = 2\pi\nu_b$, ν_b is frequency of body acceleration with ψ as a phase angle.

Electrohydrodynamics (EHD)

Blood is a complex physiological fluid consisting of haemoglobin, plasma, white blood cells, and various ionic components. Its unique composition enables it to function as an electrically conductive fluid. When the arterial walls are exposed to an electrolyte solution, a net charge is generated at the arterial walls. This leads blood to take the opposite charge near the arterial walls. The charged ion undergoes movement upon applying an electric field and subsequently induces fluid motion. This phenomenon is commonly referred to as electro-osmotic flow. The Poisson-Boltzmann equation provides the

electro-osmotic potential function, as stated in work by Manchi *et al.* [25]:

$$\nabla^2 \tilde{\Phi} = -\frac{\rho_e}{\epsilon}, \quad (20)$$

where, $\tilde{\Phi}$ is the electro-osmotic function, ϵ is dielectric constant, and ρ_e is given as:

$$\rho_e = (m^+ - m^-)e_0 z_0. \quad (21)$$

The Boltzmann distribution can effectively describe the determination of the number density of cations and anions as:

$$m^\pm = m_0 \exp\left(\mp \frac{e_0 z_0 \tilde{\Phi}}{k_B T_{avg}}\right), \quad (22)$$

where, z_0 is the charge balance, e_0 is electric constant, k_B is Boltzmann constant.

Using the Debye-Huckel linearization, the Poisson equation takes the form:

$$\left(\frac{\partial^2}{\partial r_1^{*2}} + \frac{1}{r_1^*} \frac{\partial}{\partial r_1^*} + \frac{\partial^2}{\partial z_1^{*2}}\right) \tilde{\Phi} = \frac{\tilde{\Phi}}{q_m^2}, \quad (23)$$

where $q_m = \frac{1}{e_0 z_0} \sqrt{\frac{\epsilon k_B T_{avg}}{2m_0}}$.

The boundary conditions for electro-osmotic equation are:

$$\begin{cases} \tilde{\Phi} = \tilde{\zeta}_1, & \text{at } r_1^* = R_1(z_1^*) \text{ for all } z_1^*, \\ \frac{\partial \tilde{\Phi}}{\partial r_1^*} = 0, & \text{at } r_1^* = 0 \text{ for } 0 \leq z_1^* \leq z_3, \\ \tilde{\Phi} = \tilde{\zeta}_2, & \text{at } r_1^* = R_2(z_1^*) \text{ for } z_3 \leq z_1^* \leq z_{max}. \end{cases} \quad (24)$$

2.2 Non-Dimensionalization

It is necessary to convert the governing equations presented in Eqns. (8)-(13) into dimensionless form in order to obtain a numerical solution. The introduction of non-dimensional variables is performed in the following manner:

$$\begin{aligned} \bar{u}_1^* &= \frac{L_0 u_1^*}{\delta^* U_0}, \bar{t}_1^* = \frac{U_0 t_1^*}{R_0}, \bar{z}_1^* = \frac{z_1^*}{L_0}, \bar{p}_1^* = \frac{R_0^2 p_1^*}{U_0 L_0 \mu_0}, \bar{r}_1^* = \frac{r_1^*}{R_0}, \bar{w}_1^* = \frac{w_1^*}{U_0}, \bar{\theta} = \frac{\tilde{T}^* - \tilde{T}_1^*}{\tilde{T}_w^* - \tilde{T}_1^*}, \bar{\phi} = \frac{\tilde{C}^* - \tilde{C}_1^*}{\tilde{C}_w^* - \tilde{C}_1^*}, \chi_1 = \frac{\tilde{n}^* - \tilde{n}_1^*}{\tilde{n}_w^* - \tilde{n}_1^*}, \\ \Phi &= \frac{\tilde{\Phi}}{\tilde{\zeta}_1} \bar{R}_i^* = \frac{R_i^*}{R_0} \quad (i = 1, 2), \bar{d} = \frac{d}{L_0}, \bar{r}_0 = \frac{r_0}{R_0}, \bar{z}_i = \frac{z_i}{L_0} \quad (i = 1, \dots, 4), \bar{r}_1 = \frac{r_1}{R_0}, \bar{r}_1 = \frac{\tilde{r}_1}{R_0}, Re = \frac{U_0 \rho_f R_0}{\mu_f}, M^2 = \frac{\sigma_f B_0^2 R_0^2}{\mu_f}, \\ E_1^* &= \frac{E_0}{B_0 U_0}, Gr = \frac{\rho_f R_0^2 g \gamma_f (\tilde{T}_w^* - \tilde{T}_1^*)}{\mu_f U_0}, Gc = \frac{\rho_f R_0^2 g \gamma_f (\tilde{C}_w^* - \tilde{C}_1^*)}{\mu_f U_0}, Rb = \frac{\rho_f R_0^2 g \gamma_f (\tilde{n}_w^* - \tilde{n}_1^*)}{\mu_f U_0}, Ec = \frac{U_0^2}{C_p (\tilde{T}_w^* - \tilde{T}_1^*)}, \\ Pr &= \frac{\mu_0 C_p}{k_f}, \tilde{Q} = \frac{\tilde{Q}_0 R_0^2}{\kappa_f (\tilde{T}_w^* - \tilde{T}_1^*)}, S_z = \frac{\sigma_f R_0^2 E_0^2}{\kappa_f (\tilde{T}_w^* - \tilde{T}_0^*)}, q = \frac{q_m}{R_0}, Sc = \frac{\nu}{D_m}, Pe = \frac{b W_c}{D_n}, \sigma_1 = \frac{\tilde{n}^*}{(\tilde{n}_w^* - \tilde{n}_1^*)}, \xi = \frac{R_b \rho_f R_0^2}{\mu_0}, \\ U_{hs} &= -\frac{\zeta \epsilon E_0}{\mu_0 U_0}. \end{aligned} \quad (25)$$

The aforementioned non-dimensional parameters mentioned in Eqn. (25) are inserted into the governing Eqns. (8)-(13) and removed the bars. The mild stenotic hypotheses are applied, i.e., $\delta^* (= \delta/R_0) \ll 1$, and $\epsilon (= R_0/L_0) = O(1)$. As a consequence of the aforementioned process, the governing Eqns. (8)-(13) undergo modifications, which can be expressed as follows:

Continuity Equation:

$$\frac{\partial w_1^*}{\partial z_1^*} = 0, \quad (26)$$

Momentum Equation:

r_1 -direction:

$$\frac{\partial p_1^*}{\partial r_1^*} = 0, \quad (27)$$

Z_1 -direction:

$$Re \frac{\rho_{hnf}}{\rho_f} \frac{\partial w_1^*}{\partial t_1^*} = -\frac{\partial p_1^*}{\partial z_1^*} + \frac{1}{2r_1^*} \frac{\partial}{\partial r_1^*} \left[\frac{\mu_{hnf}}{\mu_f} r_1^* \frac{\partial w_1^*}{\partial r_1^*} \right] + \frac{(\rho\gamma)_{hnf}}{(\rho\gamma)_f} \left[Gr\theta + Gc\phi - Rb\chi_1 \right] \cos \eta \delta_{ij} + U_{hs} q^2 \Phi - \frac{\sigma_{hnf}}{\sigma_f} M^2 w_1^*. \quad (28)$$

Energy Equation:

$$\frac{(\rho C_p)_{hnf}}{(\rho C_p)_f} \frac{\partial \theta}{\partial t_1^*} = \frac{1}{RePr} \frac{k_{hnf}}{k_f} \left[\frac{\partial^2 \theta}{\partial r_1^{*2}} + \frac{1}{r_1^*} \frac{\partial \theta}{\partial r_1^*} \right] + \frac{\sigma_{hnf}}{\sigma_f} \left[\frac{EcM^2}{Re} w_1^{*2} + \frac{(S_z + \tilde{Q})}{RePr} \right] + \frac{\mu_{hnf}}{\mu_f} \frac{Ec}{Re} \left[\left(\frac{\partial w_1^*}{\partial r_1^*} \right)^2 \right]. \quad (29)$$

Concentration Equation:

$$ReSc \frac{\partial \phi}{\partial t_1^*} = \frac{\partial^2 \phi}{\partial r_1^{*2}} + \frac{1}{r_1^*} \frac{\partial \phi}{\partial r_1^*} - Sc\xi\phi, \quad (30)$$

Microorganism Equation:

$$ReSb \frac{\partial \chi_1}{\partial t_1^*} = \frac{\partial^2 \chi_1}{\partial r_1^{*2}} + \frac{1}{r_1^*} \frac{\partial \chi_1}{\partial r_1^*} - Pe\sigma_1 \left(\frac{\partial \chi_1}{\partial r_1^*} \frac{\partial \phi}{\partial r_1^*} + (\sigma_1 + \chi_1) \frac{\partial^2 \phi}{\partial r_1^{*2}} \right), \quad (31)$$

Electroosmotic Equation:

$$\frac{\partial^2 \Phi}{\partial r_1^{*2}} + \frac{1}{r_1^*} \frac{\partial \Phi}{\partial r_1^*} = q^2 \Phi. \quad (32)$$

Here, Reynold's viscosity model [39] has been utilised to illustrate the temperature-dependent viscosity. The model is expressed as follows:

$$\mu_f(\theta) = \mu_0 e^{-\beta_0 \theta} = \mu_0 [1 - \beta_0 \theta] \quad \text{where } \beta_0 \ll 1 \quad (33)$$

Upon substituting dimensionless variables in Eqn. (25), the resulting modified equation for the pressure gradient can be written as:

$$-\frac{\partial p_1^*}{\partial z_1^*} = B_1 [1 + e \cos(c_1 t_1^*)], \quad (34)$$

where

$$e = \frac{D_1}{D_0}, B_1 = \frac{D_0 R_0^2}{\mu_0 U_0}, c_1 = \frac{2\pi R_0 \nu_p}{U_0}.$$

Upon applying non-dimensional values to the body acceleration Eqn. (19), the terms $F_b = \frac{\tilde{F}_b R_0^2}{\mu_0 U_0}$ and $c_2 = \frac{w_b R_0}{U_0}$ has taken the following form. The resulting form of the equation, by removing the bars, is as follows.

$$G(t_1^*) = F_b \cos(c_2 t_1^* + \psi), t_1^* > 0 \quad (35)$$

The dimensionless form of the stenosis geometry is expressed as follows:

$$R_1^*(z_1^*) = \begin{cases} 1, & 0 < z_1^* \leq d \\ 1 - \frac{6\delta^*}{5} (11(z_1^* - d) - 47(z_1^* - d)^2 + 72(z_1^* - d)^3 - 36(z_1^* - d)^4), & d < z_1^* \leq d + 1 \\ 1, & d + 1 < z_1^* \leq z_1 \\ 1 + r_1 - \sqrt{(r_1^2 - (z_1^* - z_1)^2)} & z_1 < z_1^* \leq z_2 \\ 2r_0 \sec \eta + (z_1^* - z_2) \tan \eta & z_2 < z_1^* \leq z_4 + 0.5 \\ 2r_0 \sec \eta + (z_1^* - z_2) \tan \eta - A^* & z_4 + 0.5 < z_1^* \leq z_4 + 2.5, \\ 2r_0 \sec \eta + (z_1^* - z_2) \tan \eta, & z_4 + 2.5 \leq z_1^* \leq z_{max} \end{cases} \quad (36)$$

Where $A^* = 2\delta_1^* \left\{ \cos \left(2\pi \left(\frac{z_1^* - d}{4} \right) - 0.25 \right) - 0.07 \cos \left(128\pi \left(z_1^* - d - 0.5 \right) \right) \right\} \tan(\eta)$.

The inner wall is represent as:

$$R_2^*(z_1^*) = \begin{cases} 0, & 0 < z_1^* \leq z_3, \\ \sqrt{\tilde{r}_1^2 - \left((z_1^* - z_3) - \tilde{r}_1 \right)^2}, & z_3 < z_1^* \leq z_4, \\ (z_1^* - z_2) \tan \eta, & z_4 < z_1^* \leq z_{max}. \end{cases} \quad (37)$$

The lateral junction curvature r_1 and the flow divider radius \tilde{r}_1 in the dimensionless form (after ignoring bars) are given as:

$$r_1 = \frac{1 - 2r_0 \sec \eta}{\cos \eta - 1}, \quad (38)$$

$$\tilde{r}_1 = \frac{(z_3 - z_2) \sin \eta}{(1 - \sin \eta)}, \quad (39)$$

where z_2 , z_3 and z_4 in the dimensionless form are specified as:

$$z_2 = z_1 + r_1 \sin \eta, \quad (40)$$

$$z_3 = z_2 + q_1, \quad (41)$$

and

$$z_4 = z_3 + \tilde{r}_1(1 - \sin \eta). \quad (42)$$

2.3 Radial Coordinate Transformation

In order to obtain a rectangular domain, it is necessary to apply the transformation $\left(x_1^* = \frac{r_1^* - R_2(z_1^*)}{R(z_1^*)} \right)$ to the geometry under consideration, where $R(z_1^*) = R_1(z_1^*) - R_2(z_1^*)$. Upon implementation of the aforementioned transformation, the equations denoted by Eqn. (28) through Eqn. (32) undergo a modification as follows:

$$\begin{aligned}
Re \frac{\rho_{hnf}}{\rho_f} \frac{\partial w_1^*}{\partial t_1^*} &= B_1 [1 + e \cos(c_1 t_1^*)] + \frac{1}{2} \left(\frac{1 - \beta_0 \theta}{(1 - \phi_1)^{2.5} (1 - \phi_2)^{2.5}} \right) \left[\frac{1}{R^2} \frac{\partial^2 w_1^*}{\partial x_1^{*2}} + \left(\frac{1}{x_1^* R + R_2} \right) \left(\frac{1}{R} \frac{\partial w_1^*}{\partial x_1^*} \right) \right] \\
- \frac{\beta_0}{2R^2 ((1 - \phi_1)^{2.5} (1 - \phi_2)^{2.5})} \frac{\partial w_1^*}{\partial x_1^*} \frac{\partial \theta}{\partial x_1^*} &+ \frac{(\rho\gamma)_{hnf}}{(\rho\gamma)_f} \left[Gr\theta + Gc\phi - Rb\chi_1 \right] \cos(\eta\delta_{ij}) + U_{hs} q^2 \Phi - \frac{\sigma_{hnf}}{\sigma_f} M^2 w_1^* + G(t_1^*),
\end{aligned} \tag{43}$$

$$\begin{aligned}
\frac{(\rho C_p)_{hnf}}{(\rho C_p)_f} \frac{\partial \theta}{\partial t_1^*} &= \frac{1}{RePr} \frac{k_{hnf}}{k_f} \left[\frac{1}{R^2} \frac{\partial^2 \theta}{\partial x_1^{*2}} + \left(\frac{1}{x_1^* R + R_2} \right) \left(\frac{1}{R} \frac{\partial \theta}{\partial x_1^*} \right) \right] + \frac{\sigma_{hnf}}{\sigma_f} \left[\frac{EcM^2}{Re} w_1^{*2} + \frac{S_z + \tilde{Q}}{RePr} \right] \\
&+ \frac{1}{R^2} \left(\frac{1 - \beta_0 \theta}{(1 - \phi_1)^{2.5} (1 - \phi_2)^{2.5}} \right) \frac{Ec}{Re} \left[\left(\frac{\partial w_1^*}{\partial x_1^*} \right)^2 \right],
\end{aligned} \tag{44}$$

$$ReSc \frac{\partial \phi}{\partial t_1^*} = \frac{1}{R^2} \frac{\partial^2 \phi}{\partial x_1^{*2}} + \left(\frac{1}{x_1^* R + R_2} \right) \frac{1}{R} \frac{\partial \phi}{\partial x_1^*} - Sc\xi\phi_1, \tag{45}$$

$$ReSb \frac{\partial \chi_1}{\partial t_1^*} = \frac{1}{R^2} \frac{\partial^2 \chi_1}{\partial x_1^{*2}} + \left(\frac{1}{x_1^* R + R_2} \right) \frac{1}{R} \frac{\partial \chi_1}{\partial x_1^*} - \frac{Pe\sigma_1}{R^2} \left(\frac{\partial \chi_1}{\partial x_1^*} \frac{\partial \phi}{\partial x_1^*} + (\sigma_1 + \chi_1) \frac{\partial^2 \phi}{\partial x_1^{*2}} \right), \tag{46}$$

$$\frac{1}{R^2} \frac{\partial^2 \Phi}{\partial x_1^{*2}} + \left(\frac{1}{x_1^* R + R_2} \right) \frac{1}{R} \frac{\partial \Phi}{\partial x_1^*} = q^2 \Phi. \tag{47}$$

The boundary conditions specified in Eqns. (14) and (17) have been reduced in the following manner:

$$w_1^* = 0, \quad \theta = 1, \quad \phi_1 = 1, \quad \chi_1 = 1, \quad \text{at } x_1^* = 1 \quad \text{for all } z_1^*, \tag{48}$$

$$\frac{\partial w_1^*}{\partial x_1^*} = 0, \quad \frac{\partial \theta}{\partial x_1^*} = 0, \quad \frac{\partial \phi}{\partial x_1^*} = 0, \quad \frac{\partial \chi_1}{\partial x_1^*} = 0 \quad \text{at } x_1^* = 0 \quad \text{for } 0 \leq z_1^* \leq z_3, \tag{49}$$

$$w_1^* = 0, \quad \theta = 1, \quad \phi = 1, \quad \chi_1 = 1, \quad \text{at } x_1^* = 0 \quad \text{for } z_3 \leq z_1^* \leq z_{max}. \tag{50}$$

The wall shear stress at the outer wall of the bifurcated artery is given as below:

$$\tau_w = -\frac{1}{R} \left(\frac{\partial w_1^*}{\partial x_1^*} \right)_{x_1^*=1}, \tag{51}$$

The flow rate for the parent artery and daughter artery is defined as follows:

$$Q_d^f = 2\pi R \int_0^1 w_1^* (x_1^* R + R_2) dx_1^*. \tag{52}$$

$$Q_p^f = \pi R \int_0^1 w_1^* (x_1^* R + R_2) dx_1^*. \tag{53}$$

The resistance impedance for the the parent artery and daughter artery is given by:

$$\lambda_p = \left| \frac{z_3 \left(-\frac{\partial p_1^*}{\partial z_1^*} \right)}{Q_p^f} \right|, \quad \text{for } z_1^* < z_3, \quad (54)$$

$$\lambda_d = \left| \frac{(z_{max} - z_3) \left(-\frac{\partial p_1^*}{\partial z_1^*} \right)}{Q_d^f} \right|, \quad \text{for } z_1^* \geq z_3. \quad (55)$$

The Nusselt number at the outer wall of the bifurcated artery is computed as follows:

$$Nu_x = -\frac{1}{R} \left(\frac{\partial \theta}{\partial x_1^*} \right)_{x_1^*=1}. \quad (56)$$

The Sherwood number is given as:

$$Sh_x = -\frac{1}{R} \left(\frac{\partial \phi}{\partial x_1^*} \right)_{x_1^*=1}. \quad (57)$$

Similarly, the motile density number is given as:

$$\Lambda_x = -\frac{1}{R} \left(\frac{\partial \chi_1}{\partial x_1^*} \right)_{x_1^*=1}. \quad (58)$$

3. Solution Process

It is an established fact that there are several numerical techniques to compute the partial differential equations, but the finite difference scheme is the easiest and efficient technique for finding the solution these equations. In order to solve the PDEs, we adopted the Crank-Nicolson scheme and took step size of Δx in the radial direction with a time step of $\Delta t = 0.001$ to achieve the convergence of the numerical scheme. It is also observed that further change in Δx and Δt doesn't bring any substantial changes in the results.

Discretization

The governing equations are discretized as:

$$\begin{aligned} & \left[(1 - \phi_2) \left[(1 - \phi_1) + \phi_1 \frac{\rho_{s1}}{\rho_f} \right] + \phi_2 \frac{\rho_{s2}}{\rho_f} \right] Re \left[\frac{w_i^{k+1} - w_i^k}{dt} \right] = B_1 [1 + e \cos(c_1 t^k)] \\ & \frac{1}{2} \left\{ \frac{1 - \beta_0 \theta}{(1 - \phi_1)^{2.5} (1 - \phi_2)^{2.5}} \right\} \left[\frac{1}{R^2} \left(\frac{w_{i+1}^{k+1} - 2w_i^{k+1} + w_{i-1}^{k+1}}{dx^2} + \frac{w_{i+1}^k - 2w_i^k + w_{i-1}^k}{dx^2} \right) + \frac{1}{R} \frac{1}{R x_i + R_2} \right. \\ & \left. \left(\frac{w_{i+1}^{k+1} - w_{i-1}^{k+1}}{2dx} + \frac{w_{i+1}^k - w_{i-1}^k}{2dx} \right) \right] - \frac{1}{2R^2} \left\{ \frac{\beta_0}{(1 - \phi_1)^{2.5} (1 - \phi_2)^{2.5}} \right\} \left[\left(\frac{w_{i+1}^{k+1} - w_{i-1}^{k+1}}{2dx} + \frac{w_{i+1}^k - w_{i-1}^k}{2dx} \right) \left(\frac{\theta_{i+1}^k - \theta_{i-1}^k}{2dx} \right) \right] + \\ & U_{hs} q^2 \Phi + F_b \cos(c_2 t_k + \psi) + \left[(1 - \phi_2) \left\{ (1 - \phi_1) + \phi_1 \frac{(\rho\gamma)_{s1}}{(\rho\gamma)_f} \right\} + \phi_2 \frac{(\rho\gamma)_{s2}}{(\rho\gamma)_f} \right] \left(Gr \theta_i^k + Gc \phi_i^k - Rb \chi_{1i}^k \right) \cos(\eta \delta_{ij}) - \\ & \frac{1}{2} \frac{\sigma_{nf}}{\sigma_f} M^2 (w_i^k + w_i^{k+1}) \quad (59) \end{aligned}$$

$$\left[(1 - \phi_2) \left\{ (1 - \phi_1) + \phi_1 \frac{(\rho C_p)_{s_1}}{(\rho C_p)_f} \right\} + \phi_2 \frac{(\rho C_p)_{s_2}}{(\rho C_p)_f} \right] \left[\frac{\theta_i^{k+1} - \theta_i^k}{dt} \right] = \frac{1}{RePr} \frac{k_{hnf}}{k_f} \left[\frac{1}{2R^2} \left(\frac{\theta_{i+1}^{k+1} - 2\theta_i^{k+1} + \theta_{i-1}^{k+1}}{dx^2} + \frac{\theta_{i+1}^k - 2\theta_i^k + \theta_{i-1}^k}{dx^2} \right) + \frac{1}{2(Rx_i + R_2)} \left(\frac{\theta_{i+1}^{k+1} - \theta_{i-1}^{k+1}}{2dx} + \frac{\theta_{i+1}^k - \theta_{i-1}^k}{2dx} \right) \right] + \frac{1}{R^2} \left\{ \frac{1 - \frac{\beta_0}{2}(\theta_i^{k+1} + \theta_i^k)}{(1 - \phi_1)^{2.5}(1 - \phi_2)^{2.5}} \right\} \frac{Ec}{Re} \left[\frac{1}{2} \left(\frac{w_{i+1}^{k+1} - w_{i-1}^{k+1}}{2dx} + \frac{w_{i+1}^k - w_{i-1}^k}{2dx} \right) \right]^2 + \frac{\sigma_{hnf}}{\sigma_f} \left[\left(\frac{1}{2} \frac{EcM^2}{Re} (w_i^{k+1} + w_i^k) \right)^2 + \frac{S_z + \tilde{Q}}{RePr} \right]. \quad (60)$$

$$ReSc \left[\frac{\phi_i^{k+1} - \phi_i^k}{dt} \right] = \left[\frac{1}{2R^2} \left(\frac{\phi_{i+1}^{k+1} - 2\phi_i^{k+1} + \phi_{i-1}^{k+1}}{dx^2} + \frac{\phi_{i+1}^k - 2\phi_i^k + \phi_{i-1}^k}{dx^2} \right) + \frac{1}{2(Rx_i + R_2)} \left(\frac{\phi_{i+1}^{k+1} - \phi_{i-1}^{k+1}}{2dx} + \frac{\phi_{i+1}^k - \phi_{i-1}^k}{2dx} \right) \right] - \frac{Sc\xi}{2} \left[\phi_i^{k+1} + \phi_i^k \right] \quad (61)$$

$$ReSb \left[\frac{\chi_{1i}^{k+1} - \chi_{1i}^k}{dt} \right] = \left[\frac{1}{2R^2} \left(\frac{\chi_{1i+1}^{k+1} - 2\chi_{1i}^{k+1} + \chi_{1i-1}^{k+1}}{dx^2} + \frac{\chi_{1i+1}^k - 2\chi_{1i}^k + \chi_{1i-1}^k}{dx^2} \right) + \frac{1}{2(Rx_i + R_2)} \left(\frac{\chi_{1i+1}^{k+1} - \chi_{1i-1}^{k+1}}{2dx} + \frac{\chi_{1i+1}^k - \chi_{1i-1}^k}{2dx} \right) \right] - \frac{Pe\sigma_1}{2} \left[\left\{ \frac{\chi_{1i+1}^{k+1} + \chi_{1i-1}^{k+1}}{2dx} + \frac{\chi_{1i+1}^k + \chi_{1i-1}^k}{2dx} \right\} \left(\frac{\phi_{i+1}^k - \phi_{i-1}^k}{2dx} \right) + \left\{ \sigma_1 + \frac{\chi_{1i}^{k+1} + \chi_{1i}^k}{2} \right\} \left(\frac{\phi_{i+1}^k - 2\phi_i^k - \phi_{i-1}^k}{dx^2} \right) \right] \quad (62)$$

$$\frac{\Phi_{i+1} - 2\Phi_i + \Phi_{i-1}}{dx^2} + \frac{1}{(Rx_i + R_2)} \left\{ \frac{\Phi_{i+1} - \Phi_{i-1}}{2dx} \right\} = q^2 \Phi_i \quad (63)$$

The discretized governing Eqns. (59) and (63) are then converted to a tri-diagonal system of equations, which is subsequently solved through the utilization of the Tri-Diagonal Matrix Algorithm (TDMA).

4. Results and Graphical Analysis

A MATLAB-based computer code was developed to gain insight into the mathematical and physical aspects of the current problem being considered. The code was designed to generate graphical representations of velocity, temperature, concentration, microorganisms, flow rate, impedance, Nusselt, and Sherwood profiles. This study examines the hemodynamic characteristics and blood rheology in pathological conditions such as stenosis on the arterial walls of bifurcated arteries. The thermophysical characteristics of nanoparticles and the parameters of nanofluids are shown in Tables 1,2, respectively. Table 3 (Ref. [6,10,32,34,40–45]) shows the possible values explored for the different flow parameters. Table 4 shows the numerical values of Nusselt, Sherwood, wall shear stress, and motile density numbers.

4.1 Validation

The validation of our work is consummated with the published work of Tripathi *et al.* [46]. The present study employs a finite difference methodology, specifically the Crank-Nicolson method, to compute the governing equations.

In contrast, the previously published work of [46] utilised the FTCS scheme. The present study compares two research works by analysing the impact of different parameters, namely Solutal Grashof number ($Gc = 0$), Rayleigh number ($Rb = 0$), magnetic field parameter ($M = 0$), Debye-Huckel parameter ($q = 0$), heat source ($Q = 0$), Eckert number ($Ec = 0$), and Joule heating parameter ($S_z = 0$). Additionally, the inner wall ($R_2(z) = 0$) has been considered. The velocity and temperature profile for pure blood (without the presence of nanoparticles) are illustrated in Figs. 2,3, respectively. The graphical representations illustrate a high degree of concurrence between our study and prior research [46] concerning velocity and temperature profiles.

Table 1. Thermophysical parameters of nanofluid and hybrid nanofluid.

Properties	Mathematical expression for nanofluid and hybrid nanofluid
Viscosity	$\mu_{nf} = \frac{\mu_f}{(1 - \phi_1)^{2.5}}$ $\mu_{hnf} = \frac{\mu_f}{(1 - \phi_1)^{2.5}(1 - \phi_2)^{2.5}}$
Density	$\rho_{nf} = (1 - \phi_1)\rho_f + \phi_1\rho_{s_1}$ $\rho_{hnf} = [(1 - \phi_2)\{(1 - \phi_1)\rho_f + \phi_1\rho_{s_1}\}] + \phi_2\rho_{s_2}$
Heat Capacity	$(\rho C_p)_{nf} = (1 - \phi_1)(\rho C_p)_f + \phi_1(\rho C_p)_{s_1}$ $(\rho C_p)_{hnf} = [(1 - \phi_2)\{(1 - \phi_1)(\rho C_p)_f + \phi_1(\rho C_p)_{s_1}\}] + \phi_2(\rho C_p)_{s_2}$
Thermal Conductivity	$\frac{k_{nf}}{k_f} = \frac{k_{s_1} + (m - 1)k_f - (m - 1)\phi_1(k_f - k_{s_1})}{k_{s_1} + (m - 1)k_f + \phi_1(k_f - k_{s_1})}$ $\frac{k_{hnf}}{k_{nf}} = \frac{k_{s_2} + (m - 1)k_{nf} - (m - 1)\phi_2(k_{nf} - k_{s_2})}{k_{s_2} + (m - 1)k_{nf} + \phi_2(k_{nf} - k_{s_2})}$
Electrical Conductivity	$\frac{\sigma_{nf}}{\sigma_f} = \frac{\sigma_{s_1} + (m - 1)\sigma_f - (m - 1)\phi_1(\sigma_f - \sigma_{s_1})}{\sigma_{s_1} + (m - 1)\sigma_f + \phi_1(\sigma_f - \sigma_{s_1})}$ $\frac{\sigma_{hnf}}{\sigma_{nf}} = \frac{\sigma_{s_2} + (m - 1)\sigma_{nf} - (m - 1)\phi_2(\sigma_{nf} - \sigma_{s_2})}{\sigma_{s_2} + (m - 1)\sigma_{nf} + \phi_2(\sigma_{nf} - \sigma_{s_2})}$
Thermal Expansion Coefficient	$\frac{(\rho\gamma)_{nf}}{(\rho\gamma)_f} = [(1 - \phi_1) + \phi_1 \frac{(\rho\gamma)_{s_1}}{(\rho\gamma)_f}]$ $\frac{(\rho\gamma)_{hnf}}{(\rho\gamma)_{nf}} = (1 - \phi_2)[(1 - \phi_1) + \phi_1 \frac{(\rho\gamma)_{s_1}}{(\rho\gamma)_f}] + \phi_2 \frac{(\rho\gamma)_{s_2}}{(\rho\gamma)_f}$

Table 2. Thermophysical properties of nanoparticles.

Thermophysical Properties	Blood	Al ₂ O ₃	Cu
Density [$\rho(kg/m^3)$]	1060	3970	8933
Thermal Expansion Coefficient [$\gamma \times 10^{-5}(K^{-1})$]	0.18	0.85	5
Electrical Conductivity [$\sigma(S/m)$]	0.667	3.5×10^7	10×10^{-10}
Thermal Conductivity [K (W/mK)]	0.492	40	314
Heat Capacitance [$C_p(J/kgK)$]	3770	3970	8933

Table 3. Default values of emerging parameters with their sources.

Parameters	Values	References
Magnetic field (M^2)	0–5	[6,40]
Grashof number (Gr)	0–5	[41–43]
Rayleigh number (Rb)	0–6	[32,34]
Prandtl number (Pr)	14–25	[44]
Heat source parameter (\tilde{Q})	0–1	[10,45]

4.2 Velocity Profile

The composition of blood is multifaceted, encompassing haemoglobin, plasma, white blood cells, and diverse ionic constituents. The human circulatory system consists of millions of red blood cells and other ionic components, which render it capable to exhibit biomagnetic properties. The primary objective of red blood cells (RBCs) is to transport oxygen to different tissues and organs within the human body. A comparative study was conducted to explore the impact of magnetic field parameters on the stenosed artery, motivated by its blood magnetic property. Fig. 4a depicts the velocity profile variation for different magnetic field parameter values in both parent and daughter arteries. The maximum velocity of the fluid is achieved in the absence of the magnetic field that is ($M = 0$), which reduces as the strength of the magnetic field enhances from $M = 0$ to $M = \sqrt{5}$. This has occurred due to the application of a transversal magnetic field in the direction of the flow, which produces the resistance Lorentz force and slows the fluid motion. The profile of the velocity for a variable electro-kinetic parameter, or Debye Huckel parameter q , is shown in Fig. 4b. The enhancement in the velocity profile can be explained by the electro-kinetic acceleration term present in the momentum equation, i.e., $U_{hs}q^2\Phi$. The Debye Huckel parameter is expressed as the quotient of the tube radius denoted by R_0 and the Debye length represented by q_e . It has been observed that the Debye Huckel parameter exhibits an inverse relationship with the thickness of the electric double layer (EDL). Hence, raising the value of the Debye Huckel parameter reduces the EDL width, increasing the electro-

Table 4. The numerical values of Nusselt, Sherwood, wall shear stress, and motile density numbers.

Pr	\tilde{Q}	Nu_x	ξ	Sc	Sh_x	M	Gr	τ_w	Pe	Sb	Λ_x
19	0.2	-2.7343	1.5	1.5	-0.9260	0	0.5	6.7637	0	2.5	-0.8547
23	0.2	-3.0589	2.5	1.5	-1.2907	1	0.5	6.5131	1.5	2.5	-1.5250
25	0.2	-3.2107	3	1.5	-1.4607	2	0.5	5.9094	3	2.5	-2.2929
23	0.5	-3.0156	3	1	-1.0015	2	0	4.6583	1.5	2	-1.2187
23	1	-2.9432	3	0.5	-0.5238	2	1	7.0397	1.5	1	-0.5804

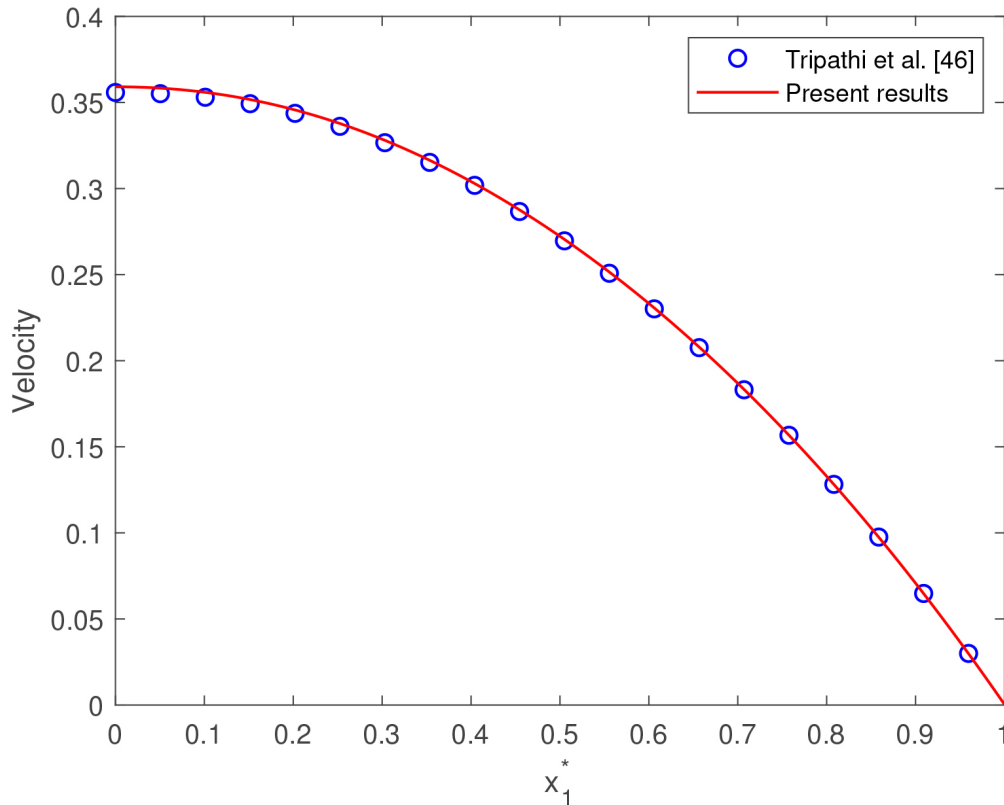


Fig. 2. Velocity profile for pure blood.

osmotic forces that counteract fluid drag and boost fluid velocity. Bioconvection phenomena can be attributed to the upward swimming of motile microorganisms in a hybrid nanofluid solution. Typically, the density of microorganisms exhibits a slightly higher value than that of the hybrid nanofluid solution, resulting in the migration of microorganisms towards the upper surface of the solution. The observed phenomenon involves generating an uneven and unstable solution, resulting in the downward displacement of microorganisms and the subsequent initiation of a bioconvection process. The association between the bioconvection Rayleigh number and the momentum equation substantially impacted the velocity profile, as seen in Fig. 4c. The increase in the Rayleigh number strengthens the microorganism's convection, which works against the buoyancy force acting on the fluid particles. This results in a decrement in the velocity profile. The variation in velocity profile by varying nanoparticle concentration is depicted in Fig. 4d. Nanoparticles play a pivotal role in facilitating the targeted delivery of therapeutic agents to specific tissues through the circulatory system, enabling the treatment of a broad spectrum of medical conditions. Upon the introduction of copper nanoparticles into the bloodstream, the blood flow velocity increases, resulting in an elevated velocity profile compared to pure blood. The figure suggests that the velocity profile reaches its maximum when introducing copper nanoparticles into the circulatory system. In contrast, the minimum velocity profile is observed in the presence of aluminium oxide nanoparticles. Thus, assisting surgeons in regulating blood flow near the diseased segment during surgical procedures. Fig. 4e illustrates the velocity profile of parent and daughter arteries by considering the different arterial cross sections. In particular, the value of $B_1 = 1.41$ corresponds to the coronary artery, whereas the value of $B_1 = 6.6$ is indicative of the femoral artery. At the stenotic position, the velocity profile displays an augmentation in its profile for increasing arterial cross section. The combined effect of the Grashof number and the solutal

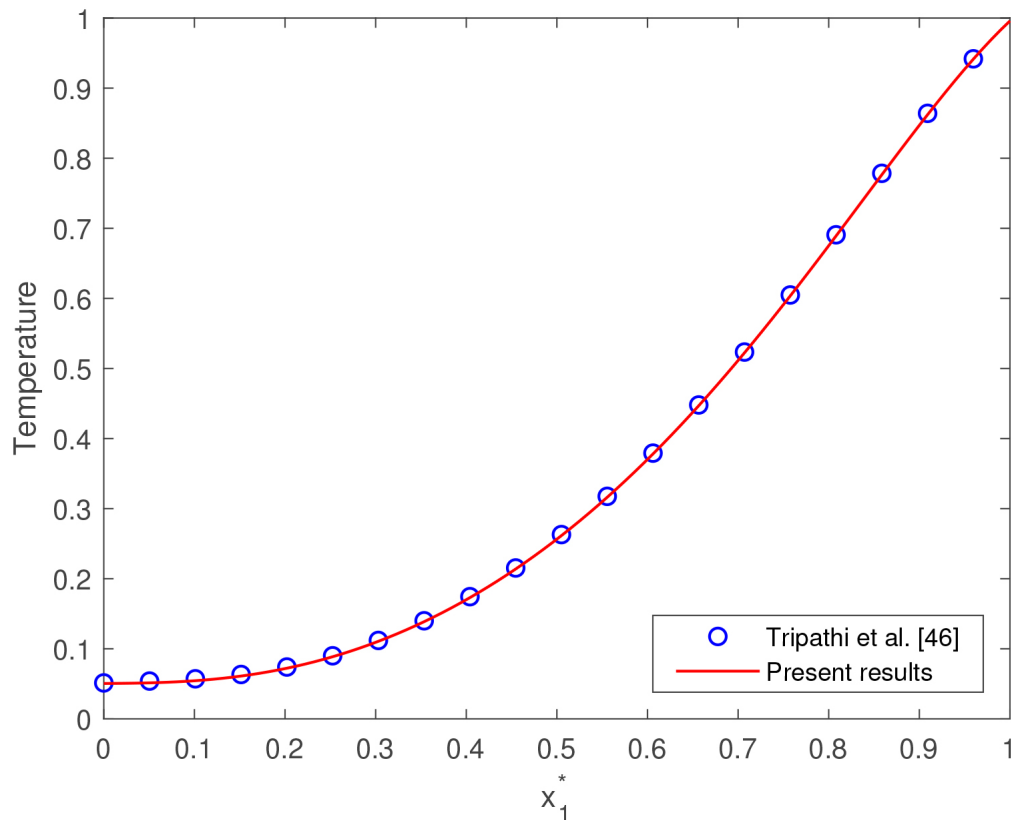


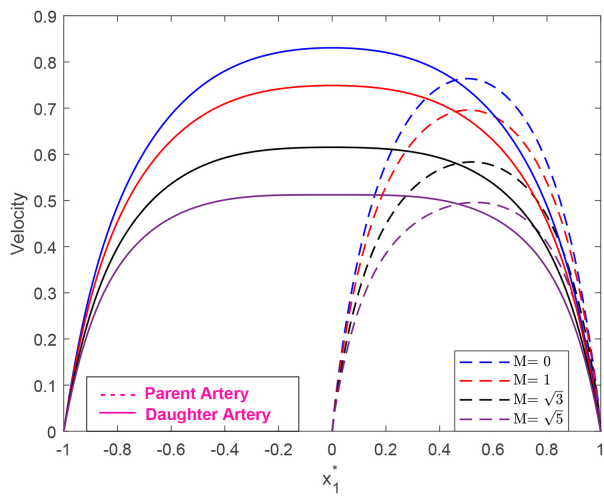
Fig. 3. Temperature profile for for pure blood.

Grashof number is depicted in Fig. 4f. Grashof number represents the ratio of buoyant force to viscous force. Clearly, it can be deduced that the fluid velocity is enhanced with an increment of Gr from 0 to 1. This has happened due to enhancement in the buoyant forces as compared to viscous forces, which accelerates the fluid velocity. A similar trend is observed for the solutal Grashof number G_c . This observed trend is corroborated in the work of Sharma *et al.* [47].

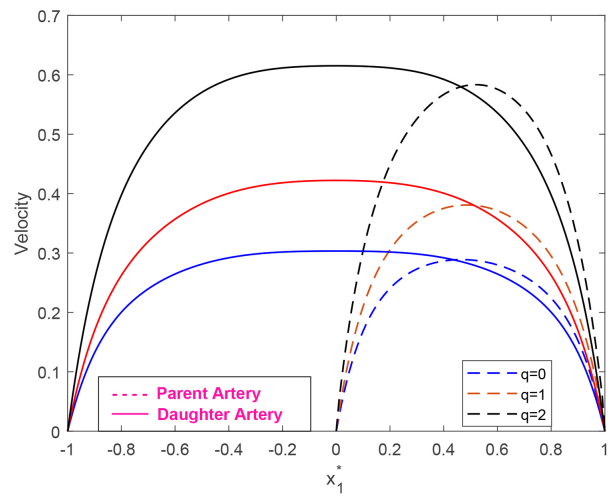
4.3 Temperature, Concentration and Microorganisms Profile

The variation in temperature for varying Prandtl number is depicted in Fig. 5a. In both the parent and daughter arteries, the temperature distribution decreases as the value of Pr enhances from 19 to 23. The Prandtl number represents the ratio of momentum and thermal diffusivity. The Prandtl value for pure blood is 21, which is higher as compared to water and other base fluids. The smaller Prandtl number has higher thermal conductivity, which signifies the heat transmitted faster from the arterial wall as compared to higher- Pr fluids. Fig. 5b signifies the argumentation in the temperature profile for an increasing heat source parameter.

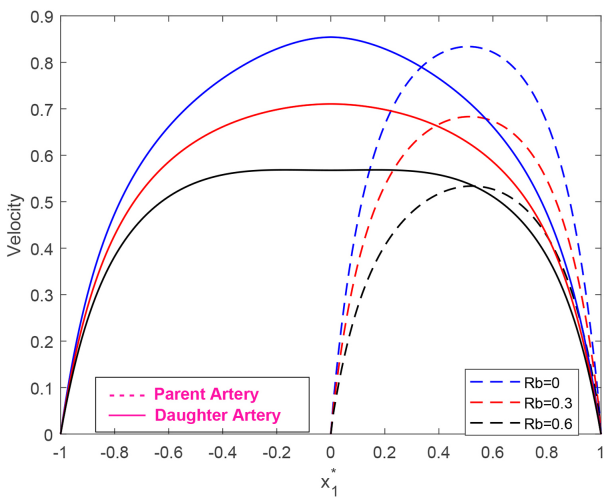
The enhancement occurs due to additional heat produced by the heat source that raises the temperature profile. The result of Fig. 5b may serve as a promising application in the drug delivery system where the metallic nanoparticles can be used as carriers to treat cancerous cells. The tumour cells present downstream of the stenotic region can be treated by enhancing the temperature. Fig. 5c,d depict the concentration profile for Schmidt and chemical reaction parameters, respectively. The concentration profile illustrates how a growing Schmidt number leads to a decreasing concentration. Sc denotes the ratio of the kinematic viscosity to the molecular diffusion coefficient. Since diffusivity is inversely proportional to Sc , a lower Sc number leads to higher diffusivity. The more highly diffusive species have a more noticeable impact of slowing down the concentration distribution. As the parameter for the chemical reaction increases, the concentration profile begins to fall. This has happened because the consumption of additional species will lead to the suppressed concentration profile. The impact of bioconvective Pe on the microorganism's distribution is seen in Fig. 5e. The Peclet number is the most prominent component that highly influences the density of microorganisms in the blood. Pe was defined as the ratio of the maximal swimming speed of a cell to the diffusion rate of microorganisms. The process by which a substance moves from an area of higher concentration to a lower concentration is commonly known as diffusion. From the figure, there is a direct correlation between the rise in the Pe value from 0 to 3, which results in a reduction in the microbes' overall dispersion. It has been discovered that an increase in the bioconvective Peclet number results in an increase in the speed of motile microorganisms, which decreases the density of microorganisms.



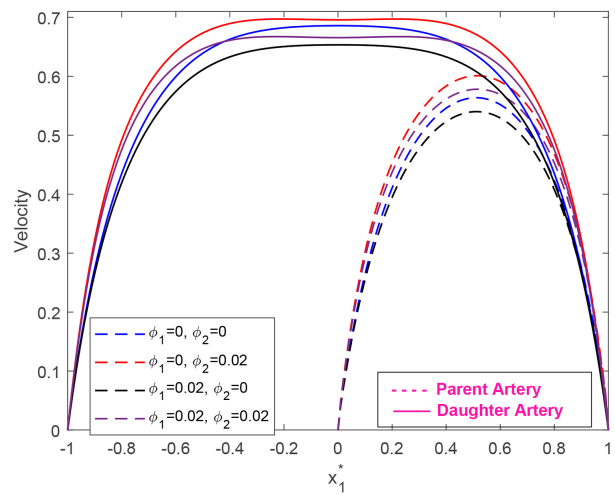
(a) Velocity profile by varying M



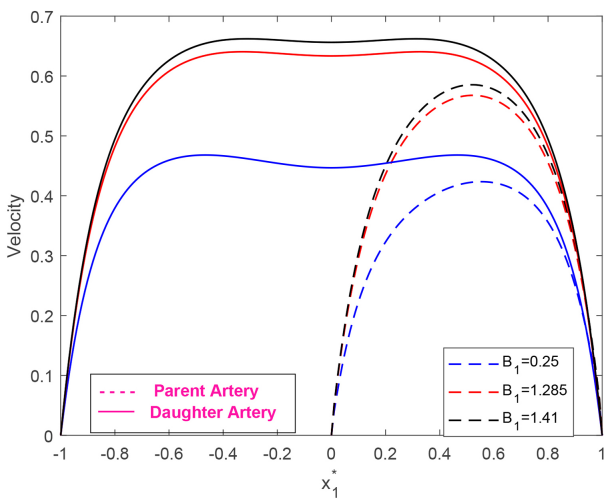
(b) Velocity profile by varying q



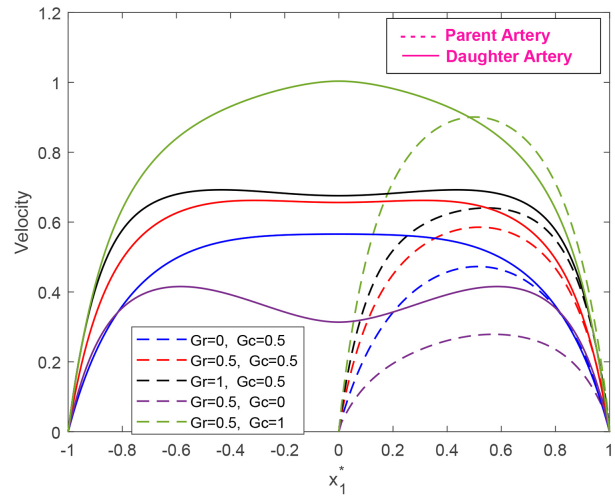
(c) Velocity profile by varying Rb



(d) Velocity profile by varying nanoparticle concentration

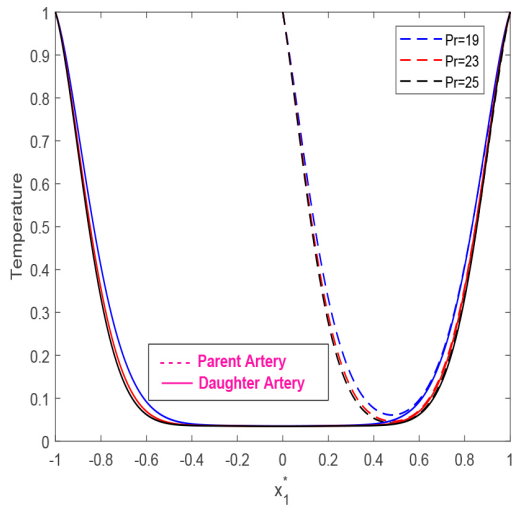


(e) Velocity profile by varying B_1

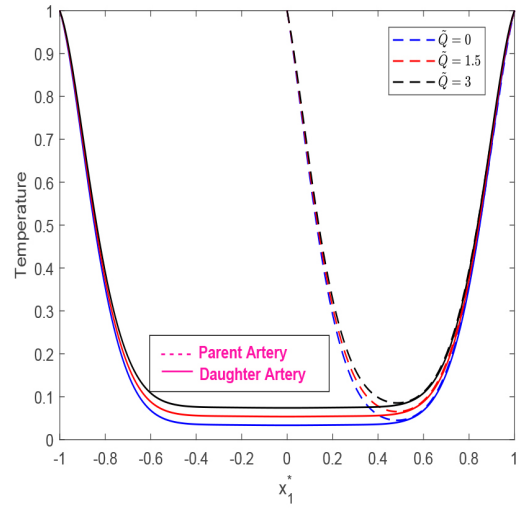


(f) Velocity profile by varying Gr and Gc

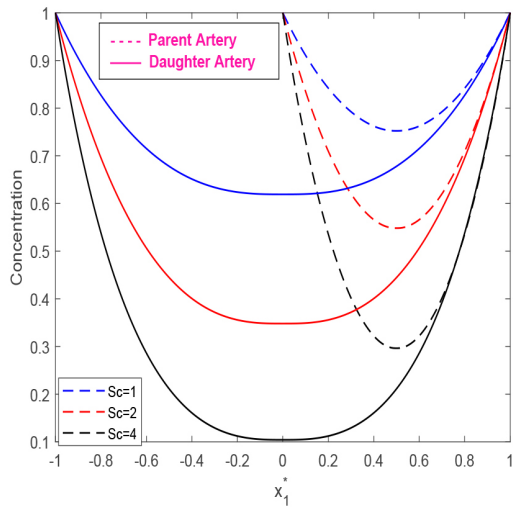
Fig. 4. Velocity profile.



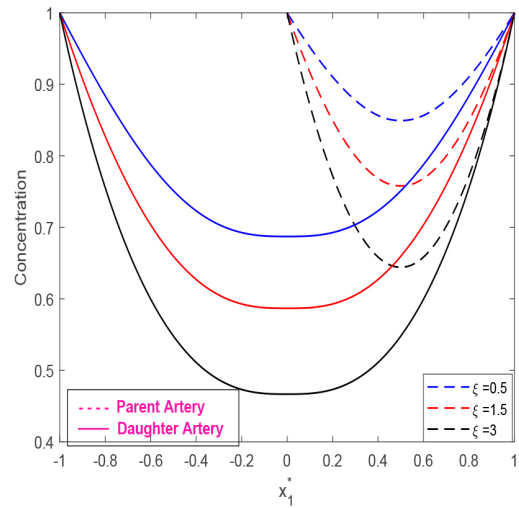
(a) Temperature profile by varying Pr



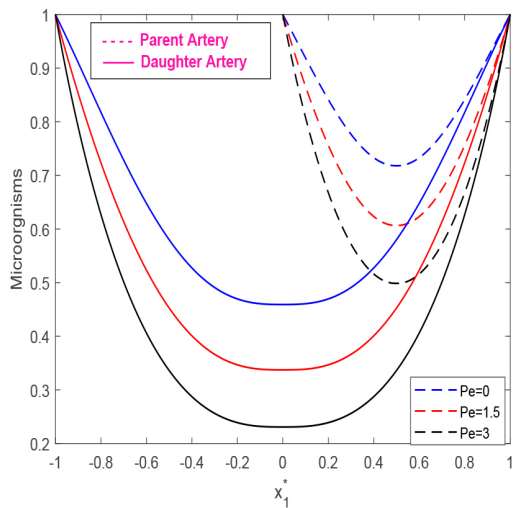
(b) Temperature profile by varying \dot{Q}



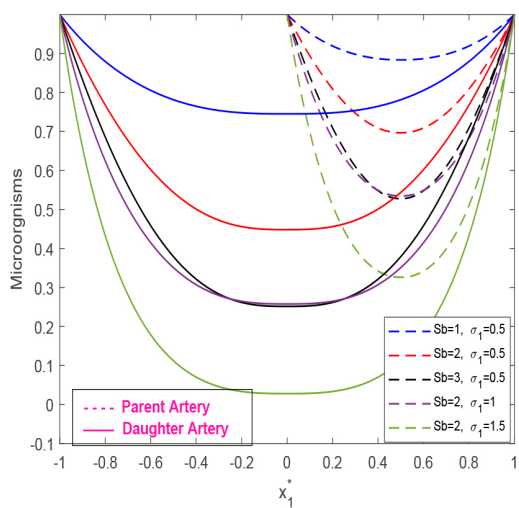
(c) Concentration profile by varying Sc



(d) Concentration profile by varying ξ

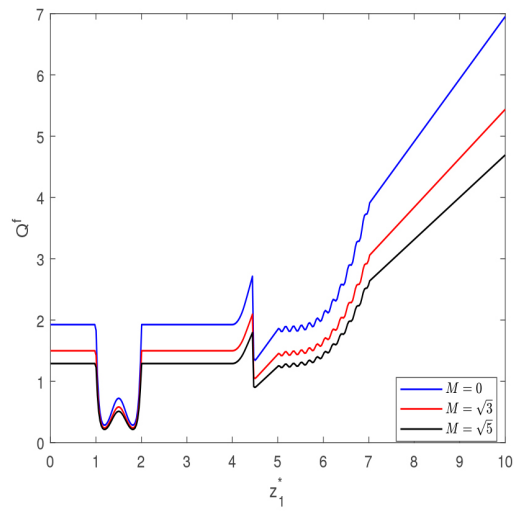


(e) Microorganisms profile by varying Pe

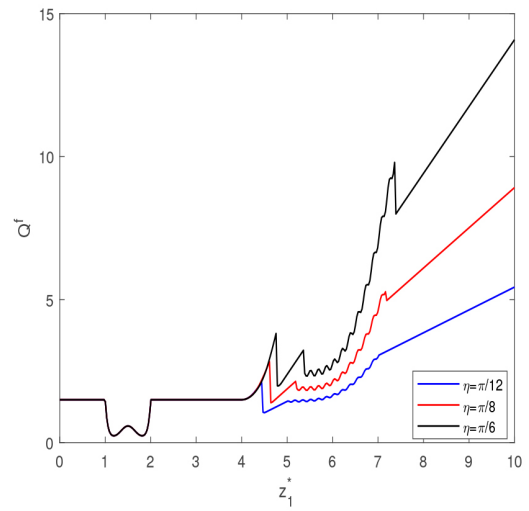


(f) Microorganisms profile by varying Sb

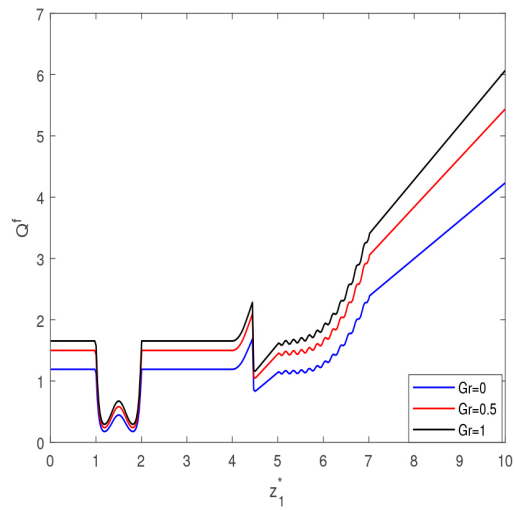
Fig. 5. Temperature, Concentration and Microorganisms profile.



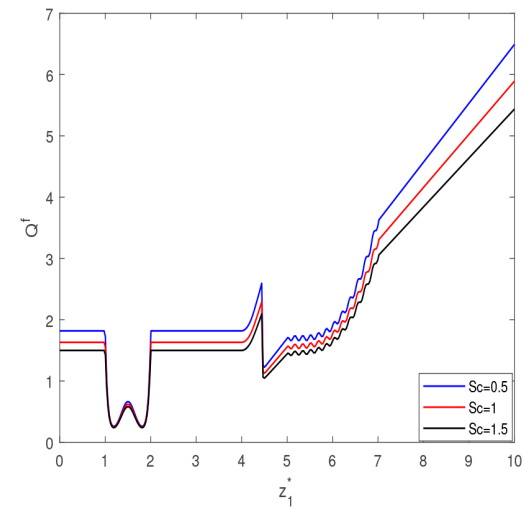
(a) Flow rate profile for varying M



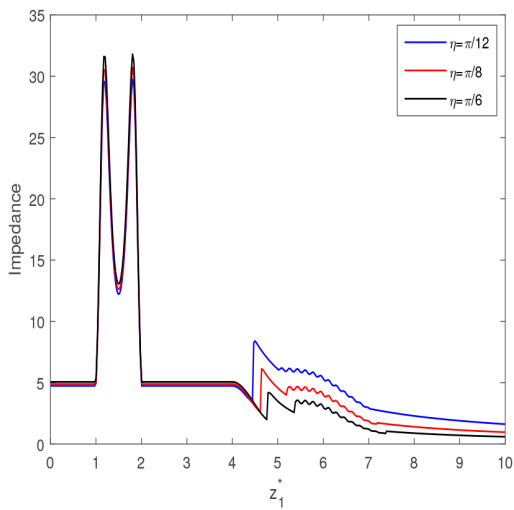
(b) Flow rate profile for varying η



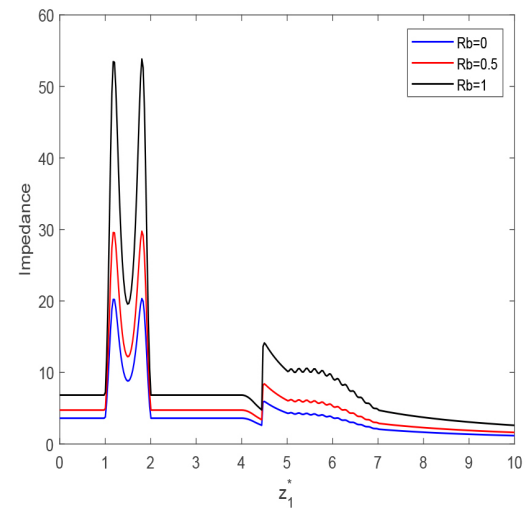
(c) Flow rate profile for varying Gr



(d) Flow rate profile for varying Sc

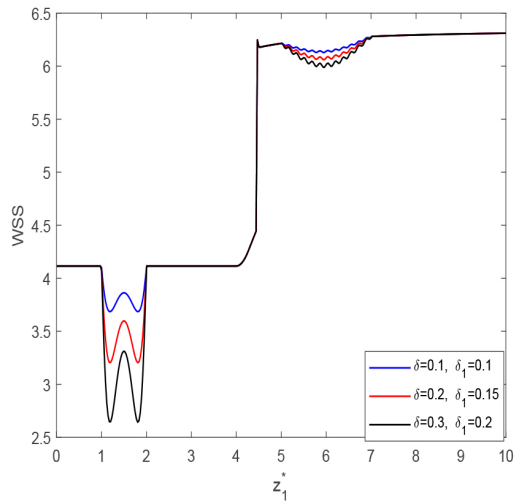


(e) Impedance profile by varying η

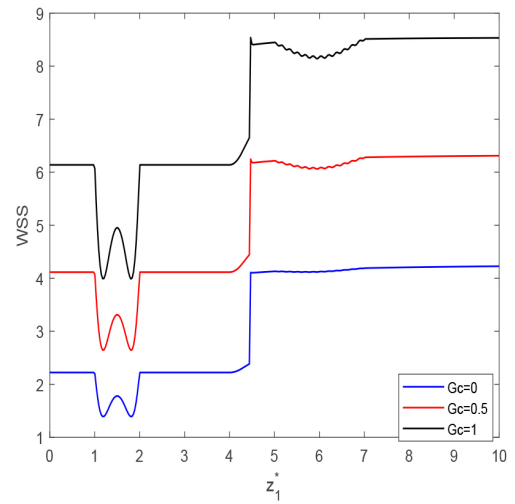


(f) Impedance profile by varying Rb

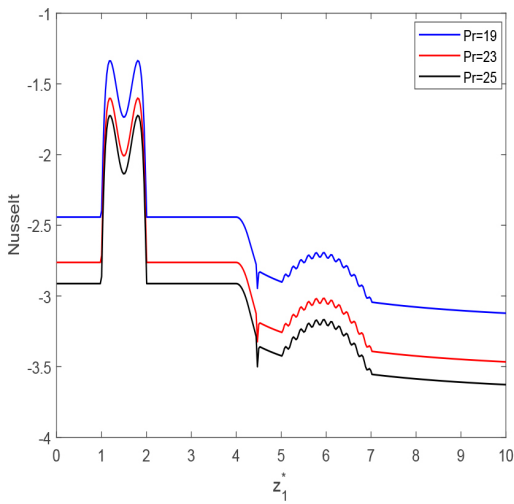
Fig. 6. Flow rate and Impedance profile.



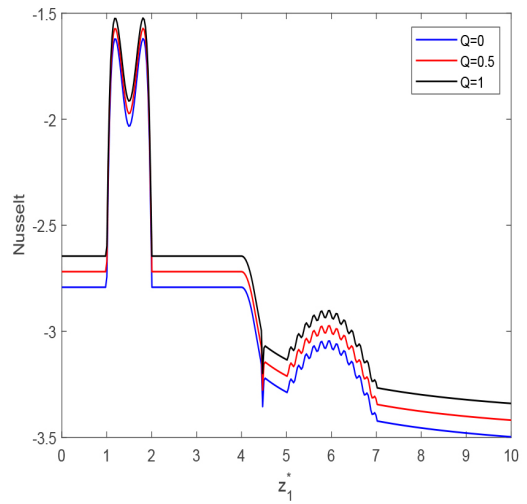
(a) Wall shear stress by varying stenotic depth



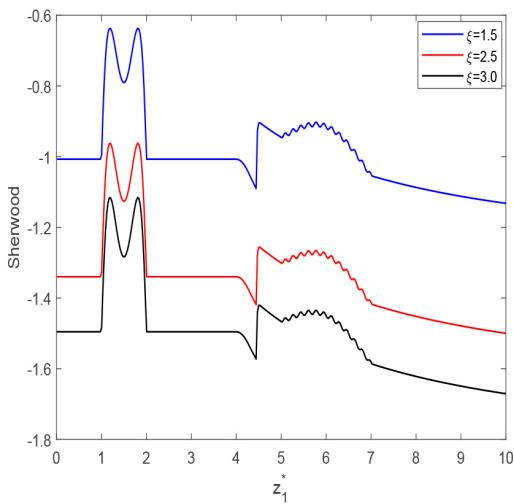
(b) Wall shear stress by varying Gc



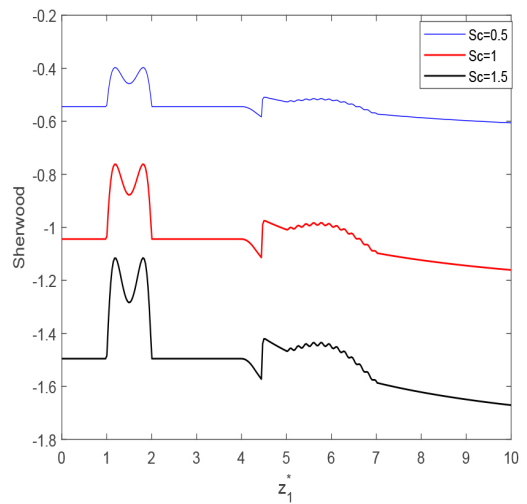
(c) Nusselt profile varying Pr



(d) Nusselt profile varying Q



(e) Sherwood profile by varying ξ



(f) Sherwood profile by varying Sc

Fig. 7. WSS, Nusselt number and Sherwood profile. WSS, wall shear stress.

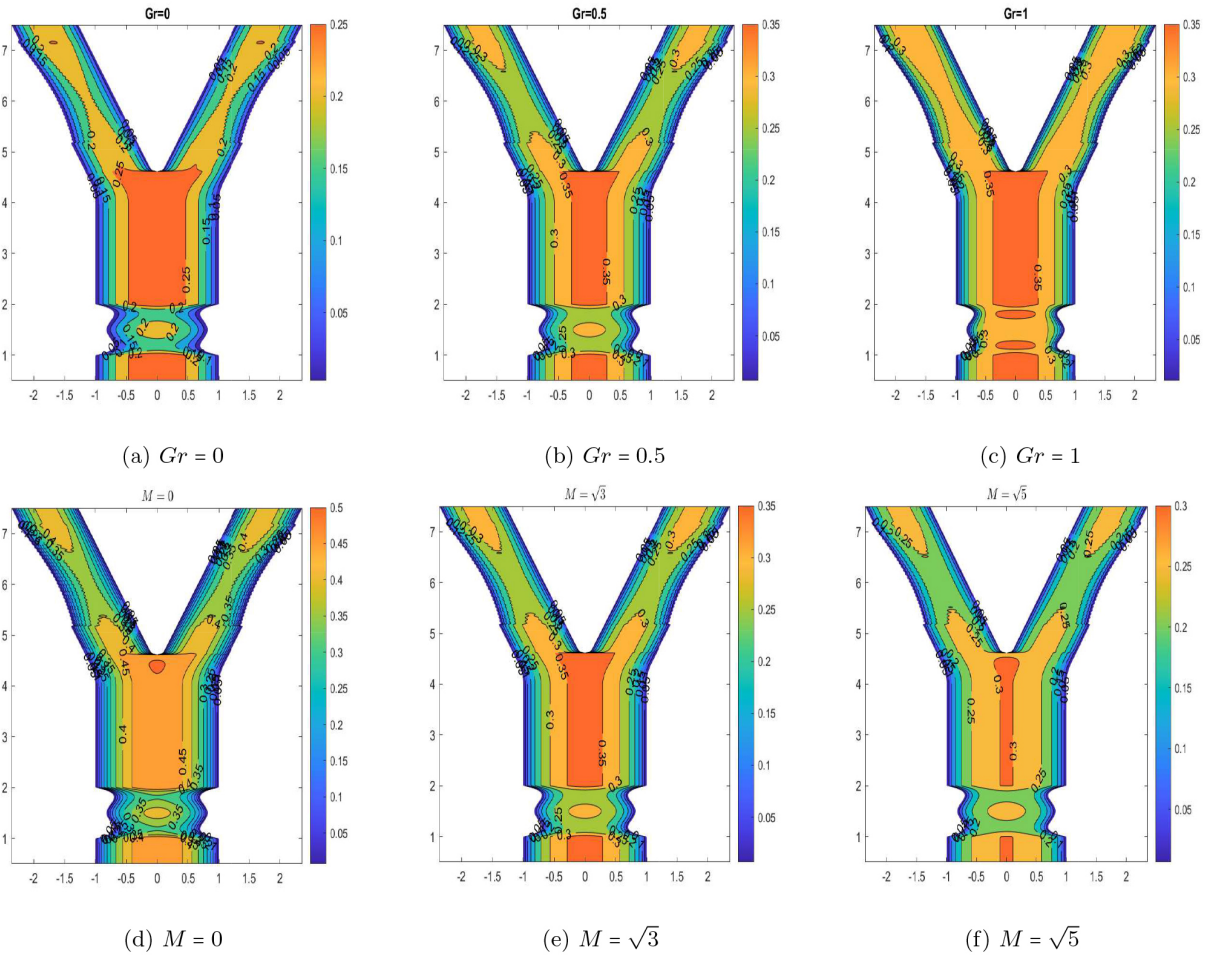


Fig. 8. Velocity contour for Grashof number and Magnetic field parameter.

The combined impact of the bioconvective Lewis number and the microbial concentration differences parameter on the dispersion of microorganisms is shown in Fig. 5f. The figure shows that the density decreases for an upsurge in magnitude of parameter σ_1 . This results from a more significant density differential being formed between the gyrotactic microorganisms and the base fluid, which causes the gyrotactic bacteria to flow back and suppresses the concentration profile. The mounting value of Sb reduces the motile density of the fluid, and this has happened due to a decrease in the microorganism's diffusivity process. This shows that the microorganism's density reduces in both sections of the bifurcated artery (parent and daughter arteries) as the magnitude of Sb and σ_1 enhances.

4.4 Flow Rate & Impedance Profile

In stenotic conditions, the hemodynamic factors play a crucial role in assessing the risk of atherosclerosis progression induced by flow disorders. Thus, it is essential to study these factors to reduce its risk and address it at the correct time for better treatment. The volumetric flow rate is defined as the amount of fluid that passes through the arteries in a given amount of time. In contrast, fluid resistance, known as Impedance, is determined by the ratio of pressure drop to flow rate. Fig. 6a shows the flow rate profile for varying magnetic field parameters. The flow rate profile depicts the declining nature as the magnetic field parameter enhances from $M = 0$ to $M = \sqrt{5}$. The flow rate is maximum in the absence of a magnetic field ($M = 0$), which clearly shows that the flow rate can be regulated by the magnetic field. The fluid experiences the resistive Lorentz force that retard the fluid motion, and from the figure; it can also be interpreted that the fluid experiences the disturbance at the bifurcated point. Fig. 6b illustrates the flow rate change when the bifurcation angle is changed from $\pi/12$ to $\pi/6$. According to the inferences drawn from the figure, the flow rate profile remains unchanged in the parent artery but undergoes substantial changes following the bifurcation. The daughter artery's flow rate profile increases with enhancement in the bifurcation angle. The flow rate as a function of the Grashof number is seen in Fig. 6c. This results from an increase in the temperature differential between the two regions, which has caused the buoyant force to predominate compared to the viscous forces. As a consequence, there has been an increase in the flow rate profile. The decrease in flow

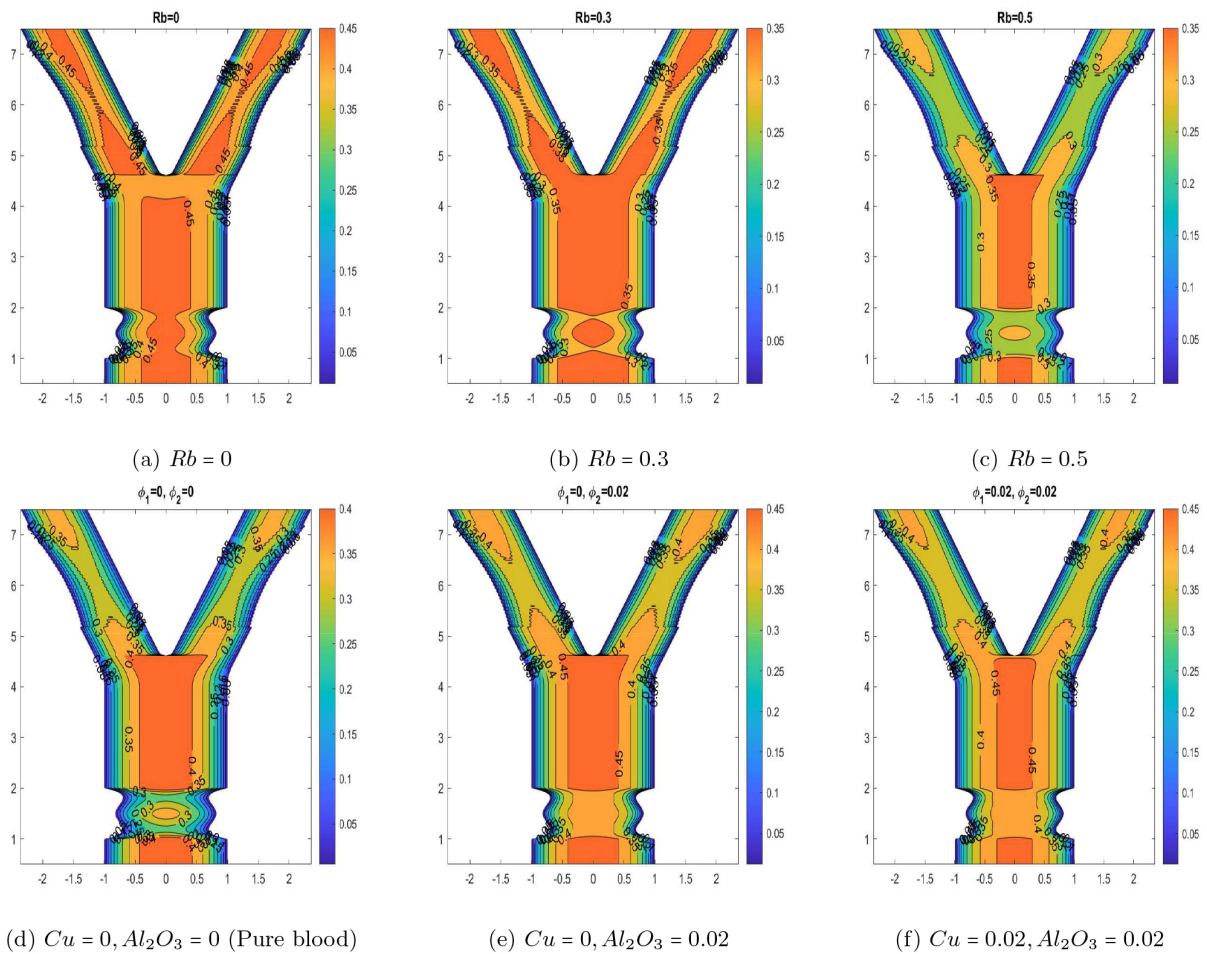


Fig. 9. Blood flow pattern for Rayleigh number and nanoparticle volumetric concentration.

rate that occurs when the value of the Schmidt number grows from 0.5 to 1.5 is seen in Fig. 6d. The reduction in molecular diffusion is shown physically by an increase in the value of Sc , whereas a reversal of behaviour was seen concerning the velocity profile, which led to a drop in the flow rate profile. Fig. 6e illustrates the decrement in the velocity profile as the bifurcated angle increases from $\pi/12$ to $\pi/6$. It can be observed that for change in the bifurcation angle, the impedance profile depicts no change in the parent artery but shows the changes in the daughter artery as the bifurcated angle caused the fluid to change its behaviour and led to the decreasing profile for an increasing bifurcation angle. Fig. 6f shows the growing nature of the impedance profile by enhancing the Rayleigh number. The impedance profile is minimum when $Rb = 0$ and increases for a positive value of Rb . It has been noticed that the convection produced by microorganisms lowers the buoyant force that hinders the mobility of the fluid and raises the impedance distribution.

4.5 WSS, Nusselt Number and Sherwood Number

Wall shear stress (WSS) is defined as the force per unit area on the fluid produced by the arterial wall along the tangential direction. The research concluded that WSS is a critical component in the biomedical industry for elucidating the pattern of atherosclerotic lesion development. This research has clinical potential for assessing WSS's temporal and spatial distribution, which may aid in the early diagnosis of stenosis. Fig. 7a depicts the WSS distribution by illustrating the effect of varying the stenotic depth in the bifurcated artery. In both sections of the arteries (parent and daughter arteries), the WSS profile decreases as the stenotic depth increases. The findings of this research corroborate those of Zhang's experimental work [48], which also found that arterial lesion development decreased WSS. Fig. 7b indicates the influence of the solutal Grashof number on the WSS profile. The study reveals that the WSS profile rises as the parameter Gc increases from 0 to 1. WSS profile shows the minimum profile when $Gc = 0$ and increases as the Gc enhances, leading to the emergence of a buoyant force that improves the flow near the arterial wall and enhances the WSS profile. Table 4 illustrates the reduction in the wall shear stress (τ_w) profile with an escalation in M , whereas the converse pattern is discernible for Gr . The parameter τ_w experiences an augmentation from 4.65 to 7.03 as the Gr value ascends from 0 to 1. Conversely, τ_w exhibits a decrement

from 6.76 to 5.90 as the magnetic field parameter (M) progresses from 0 to 2. The ratio of convective heat transmission to conductive heat transfer in the arterial walls is represented by the dimensionless Nusselt number. The decrease in the Nusselt number that occurs with an increasing Prandtl number is seen in Fig. 7c and Table 4. It can be inferred from the figure that the efficiency of transferring heat from the arterial wall to blood reduces as the Pr value enhances. This has happened due to the low thermal conductivity of higher-Pr fluids. Fig. 7c visually represents the relationship between the Nusselt and Prandtl numbers. The figure demonstrates that as the Prandtl number increases, there is a notable decrease in the Nusselt number. The observed pattern indicates that heat transfer efficiency from the arterial wall to the blood decreases as the Prandtl values increase.

In the context of arterial heat transfer, it has been observed that fluids with higher Prandtl numbers tend to demonstrate diminished efficacy in the conduction of heat compared to fluids with lower Prandtl numbers. Consequently, the Nusselt number decreases with increasing Prandtl number, indicating a reduced ability to transfer heat from the arterial wall to the blood. Fig. 7d and Table 4 depict the relation between the heat source parameter and the Nusselt profile. The utilisation of a heat source has been found to have potential applications in therapeutic procedures. By selectively targeting the affected region, heat energy can be generated without causing harm to nearby tissues. This localised heating can serve multiple purposes, including the dilation of arteries to facilitate increased blood flow to the affected area. Therefore, it can be utilised as a potential intervention to mitigate stenosis. From the Fig. 7d, it can be inferred that there is an apparent upward trend in the Nusselt profile associated with an escalation in the heat source parameter. An increase in the heat source parameter from 0 to 1 induces a rise in the heat generation rate within the blood, thereby causing an escalation in the temperature, enhancing the Nusselt number profile. Similarly, the Table 4 show the enhancement in the Nusselt profile as the heat source parameter increases from 0.2 to 1 at the axial position $z_1^* = 6.12$.

Thermal treatment is one of the finest ways to expose blood tissue and cancerous cells to high temperatures in biomedical area; nevertheless, it must be performed under safety recommendations to prevent damage to healthy tissues. The effect of the chemical reaction parameter and Schmidt number on the Sherwood profile is demonstrated in Fig. 7e,f, respectively. The statistics suggest that nature is deteriorating, with a rise in ξ and Sc . This pattern may be described by the fact that the molecular diffusivity lowers, indicating a lesser mass transfer across the wall, which leads to a diminishing nature in the Sherwood profile. Table 4 presents the numerical values of the Sherwood profile for ξ and Sc at the axial position $z_1^* = 6.12$. The table illustrates the decrease in the Sherwood profile as the values of Sc and ξ increase. Additionally, Table 4 depicts the variation in the motile density number Λ_x with increasing values of Pe and Sb . Clearly, it can be inferred that the Λ_x profile decreases with an increase in the parameters Pe and Sb , resulting from a reduction in the microorganism's density.

4.6 Velocity Contour

This section presents visual representations of the velocity pattern as influenced by various parameters. This facilitates an enhanced visual and comprehensive depiction of the hemodynamic flow in close proximity to the constricted area along the walls of the bifurcated artery.

The velocity contour for varying Grashof numbers is depicted in Fig. 8a–c. The figure demonstrates a positive correlation between the elevation of the trapping bolus and the magnitude of Gr . The maximum velocity achieved is 0.35 for both scenarios when the Grashof number (Gr) is equal to 0 and 0.5. Additionally, a maximum velocity of 0.25 is explicitly observed for the case when Gr is equal to 0. The maximum fluid speed is observed to occur in the parent region for all three cases. This phenomenon is attributed to the reduction in the value of Gr in the daughter artery, which is caused by the inclination angle $\eta/2$. The velocity contour demonstrates the relationship between the augmentation in velocity and the accompanying elevation in Gr , which can be ascribed to the amplification of the buoyant thermal force and its subsequent influence on the velocity profile. The effect of the magnetic field on the velocity contour is seen in Fig. 8. Fig. 8d–f show that the velocity field decreases when the magnetic field parameter increases. Without a magnetic field, the fluid can only reach a maximum speed of 0.5, but when the magnetic field parameter is enhanced, the fluid's speed reduces. The resistive Lorentz force is responsible for the declination in the velocity, which can be predicted by the velocity contour.

The velocity contour for different values of Rb is depicted in Fig. 9a–c. The data suggest a negative correlation between velocity and Rb , indicating that an increase in Rb results in a decrease in velocity. In the context of Rb deficiency, it has been noted that the maximum velocity profile is achieved in both the parent and daughter arteries. According to our findings, maximum resistance resulting from the overlapping stenosis occurs at $Rb = 0.3$. In the region pertaining to the daughter, a decrease in the quantity of trapped bolus is observed as the value of Rb varies from 0.3 to 0.5. The presence of overlapping and irregular stenosis is observed to cause resistance and decrease fluid velocity in the vicinity of the affected segments. The observed decrease in velocity profile can be attributed to the strengthening of Rb , which resulted in the microorganism's convection counteracting the buoyancy force exerted on the fluid particles.

Fig. 9d–f displays the velocity contour related to manipulating volumetric nanoparticle concentration. The maximum velocity achievable by pure blood has been found to be 0.4. Additionally, the presence of trapped bolus can be observed in the vicinity of overlapping stenosis. Upon insertion of the copper nanoparticle into the bloodstream, there is an observed

increase in the maximum velocity of the fluid, as illustrated in the Fig. 9e. Fig. 9f depicts the velocity contour of copper and aluminium oxide suspended in the base fluid (blood). Although the maximum velocity remains constant in both cases Fig. 9e and Fig. 9f, the velocity profile is reduced when aluminium oxide nanoparticles are doped in copper/blood solution. These findings provide novel insights for evaluating the precision of theoretical investigations on complex systems and comprehending the impact of blood properties on diverse nanoparticles. Consequently, the surgeon surgeon possesses the ability to regulate the blood flow during the surgical intervention.

5. Conclusions

The current study presents a mathematical model describing the hemodynamic flow through a bifurcated artery with overlapping and irregular stenosis at the parent and daughter arteries, respectively. The investigation has focused on implementing the $\text{Al}_2\text{O}_3\text{-Cu}$ /Blood hybrid nanofluid in conjunction with electroosmotic force, a heat source, and microorganisms. Nanoparticles are colloidal suspensions composed of microscopic-shaped substances dispersed in a base fluid. The favourable heat transfer capabilities and stability of nanofluids make them an ideal choice for applications in the biomedical field. The pursuit of stable, non-aggregating, and bio-compatible medicines is a primary objective of researchers. The antibacterial and antiviral properties of copper nanoparticles are attributed to their large surface area-to-volume ratio. The chemical stability of aluminium oxide nanoparticles (AINPs) in abrasive environments, their low cost, and ease of acquisition render them a viable option for application in biomedicine. The favourable characteristics exhibited by the nanoparticles have prompted us to investigate the potential of utilising the $\text{Al}_2\text{O}_3\text{-Cu}$ /Blood hybrid nanofluid in the context of the bifurcated artery. The significant outcomes are outlined below:

- It is noticed that the velocity profile decreases in both parent and daughter artery with enhancement in magnetic field parameter while reverse trend is observed for Debye-Huckel parameter.
- Temperature profile enhances with an upsurge in the heat source parameter.
- The mounting value of S_b reduces the motile density of the fluid, attributed to a reduction in microorganism diffusivity.
- Nusselt number profile decline with an enhancement in Pr while the opposite behaviour is observed for heat source parameter.
- Sherwood profile decreases with an enhancement in both chemical reaction parameter and Schmidt number due to lower molecular diffusivity.

The future scope of this study includes extending the investigation to incorporate solute dispersion in the Darcy-Brinkman-Forchheimer porous medium with compliant walls. Additionally, the temperature-dependent viscosity model employed in this study can be substituted with a hematocrit-dependent viscosity model. Further exploration can involve replacing the Newtonian fluid with a non-Newtonian fluid and incorporating the influence of nanoparticle size. Additionally, the wall conditions can be modified to include velocity-slip and thermal-slip conditions.

Availability of Data and Materials

The datasets used and/or analyzed during the current study available from the corresponding author on reasonable request.

Author Contributions

UK—drafting the manuscript, methodology, investigation, software handling, review and editing; BKS—conceptualization, drafting the manuscript, review and editing; BA—analysis, interpretation of data, review and editing; MMB—methodology, investigation, software handling, interpretation of data. All authors contributed to editorial changes in the manuscript. All authors read and approved the final manuscript. All authors have participated sufficiently in the work and agreed to be accountable for all aspects of the work.

Ethics Approval and Consent to Participate

Not applicable.

Acknowledgment

The research is supported by Researchers Supporting Project number (RSP2024R158), King Saud University, Riyadh, Saudi Arabia.

Funding

The research is supported by Researchers Supporting Project number (RSP2024R158), King Saud University, Riyadh, Saudi Arabia.

Nomenclature

u_1^*	Radial velocity (ms^{-1})	f_p	Heart pulse frequency
w_1^*	Axial direction (ms^{-1})	Gr	Thermal Grashof Number
z_1^*	Axial direction (m)	Gc	Solutal Grashof Number
r_1^*	Radial direction (m)	Ec	Eckert Number
U_0	Reference velocity (ms^{-1})	Q_p^f, Q_d^f	Volumetric flow rate in parent and daughter artery (m^3/s)
\tilde{T}^*	Temperature (K)	e	Systolic to diastolic pressure ratio
\tilde{C}^*	Concentration (K)	Rb	Rayleigh number
g	Acceleration due to gravity (ms^{-2})	Pr	Prandtl Number
t_1^*	Time (s)	k_f	Thermal conductivity ($\text{W}/(\text{m}\cdot\text{K})$)
\tilde{T}_1^*	Reference Temperature (K)	Greek letters	
\tilde{T}_w^*	Temperature at wall (K)	$(C_p)_{hnf}$	Specific heat at constant pressure ($\text{J Kg}^{-1} \text{K}^{-1}$)
\tilde{C}_1^*	Reference Concentration (mol m^{-3})	σ	Electrical conductivity (S/m)
\tilde{C}_w^*	Concentration at wall (mol m^{-3})	δ_i	Stenosis depth (m)
f_b	Frequency of body acceleration	ρ_{nf}	Density of nano-fluid (Kg/m^3)
R_0	Radius of normal artery (m)	τ_w	Shear stress at the wall (Pa)
\tilde{Q}	Heat Source parameter	λ	Impedance (Ω (Ohm))
\mathbf{B}	Uniform Magnetic Field (T)	ω_b	Circular frequency
Re	Reynold's Number	μ_f	Blood's viscosity (Pa-s)
F_b	Body acceleration parameter	μ_0	Reference viscosity (Pa-s)
D_0	Amplitude of pulsatile component	γ	Thermal expansion coefficient (K^{-1})
D_1	Amplitude of pressure gradient		

Conflict of Interest

The authors declare no conflict of interest.

References

- [1] Young DF. Effect of a time-dependent stenosis on flow through a tube. *Journal of Manufacturing Science and Engineering*. 1968; 90: 248–254.
- [2] Akbar NS, Nadeem S, Hayat T, Hendi AA. Effects of heat and chemical reaction on Jeffrey fluid model with stenosis. *Applicable Analysis*. 2012; 91: 1631–1647.
- [3] Shit GC, Roy M. Effect of induced magnetic field on blood flow through a constricted channel: An analytical approach. *Journal of Mechanics in Medicine and Biology*. 2016; 16: 1650030.
- [4] Tripathi B, Sharma BK. Two-phase analysis of blood flow through a stenosed artery with the effects of chemical reaction and radiation. *Ricerche di Matematica*. 2021; 1–27.
- [5] Khanduri U, Sharma BK. Hall and ion slip effects on hybrid nanoparticles (Au-GO/blood) flow through a catheterized stenosed artery with thrombosis. *Proceedings of the Institution of Mechanical Engineers, Part C: Journal of Mechanical Engineering Science*. 2023; 237: 2256–2278.
- [6] Khanduri U, Sharma BK. Mathematical Analysis of Hall Effect and Hematocrit Dependent Viscosity on Au/GO-Blood Hybrid Nanofluid Flow Through a Stenosed Catheterized Artery with Thrombosis. In *International workshop of Mathematical Modelling, Applied Analysis and Computation* (pp. 121–137). Cham: Springer Nature Switzerland. 2022.
- [7] Tan YB, Mustapha N, Sarifuddin. Blood flow through a stenosed artery bifurcation under the effects of gravity. *AIP Conference Proceedings*. American Institute of Physics. 2014; 1635: 241–248.
- [8] Srinivasacharya D, Madhava Rao G. Modeling of Blood Flow through a Bifurcated Artery Using Nanofluid. *BioNanoScience*. 2017; 7: 464–474.
- [9] Srinivasacharya D, Rao GM. Pulsatile flow of couple stress fluid through a bifurcated artery. *Ain Shams Engineering Journal*. 2018; 9: 883–893.
- [10] Shahzadi I, Suleman S, Saleem S, Nadeem S. Utilization of Cu-nanoparticles as medication agent to reduce atherosclerotic lesions of a bifurcated artery having compliant walls. *Computer Methods and Programs in Biomedicine*. 2020; 184: 105123.
- [11] Shahzad H, Wang X, Ghaffari A, Iqbal K, Hafeez MB, Krawczuk M, *et al*. Fluid structure interaction study of non-Newtonian Casson fluid in a bifurcated channel having stenosis with elastic walls. *Scientific Reports*. 2022; 12: 12219.
- [12] Kolin A. *An Electromagnetic Flowmeter. Principle of the Method and its Application to Bloodflow Measurements*. *Experimental Biology and Medicine*. 1936; 35: 53–56.
- [13] Ahmed A, Nadeem S. Effects of magnetohydrodynamics and hybrid nanoparticles on a micropolar fluid with 6-types of stenosis. *Results in Physics*. 2017; 7: 4130–4139.
- [14] Majekodunmi Joshua T, Anwar K, Abdullah N. Numerical Study of Magnetohydrodynamic Blood Flow through an Artery with Multiple Stenosis. *IOP Conference Series: Materials Science and Engineering*. 2020; 864: 012199.
- [15] Kumar D, Satyanarayana B, Kumar R, Kumar S, Deo N. Application of heat source and chemical reaction in MHD blood flow through

permeable bifurcated arteries with inclined magnetic field in tumor treatments. *Results in Applied Mathematics*. 2021; 10: 100151.

- [16] Manchi R, Ponalagusamy R. Modeling of pulsatile EMHD flow of Au-blood in an inclined porous tapered atherosclerotic vessel under periodic body acceleration. *Archive of Applied Mechanics*. 2021; 91: 3421–3447.
- [17] Sharma BK, Kumawat C, Makinde OD. Hemodynamical analysis of MHD two phase blood flow through a curved permeable artery having variable viscosity with heat and mass transfer. *Biomechanics and Modeling in Mechanobiology*. 2022; 21: 797–825.
- [18] Mishra NK, Sharma M, Sharma BK, Khanduri U. Soret and Dufour effects on MHD nanofluid flow of blood through a stenosed artery with variable viscosity. *International Journal of Modern Physics B*. 2023; 37: 2350266.
- [19] Sharma M, Sharma BK, Khanduri U, Mishra NK, Noeiaghdam S, Fernandez-Gamiz U. Optimization of heat transfer nanofluid blood flow through a stenosed artery in the presence of Hall effect and hematocrit dependent viscosity. *Case Studies in Thermal Engineering*. 2023; 47: 103075.
- [20] Mekheimer KS, Shahzadi I, Nadeem S, Moawad AMA, Zaher AZ. Reactivity of bifurcation angle and electroosmosis flow for hemodynamic flow through aortic bifurcation and stenotic wall with heat transfer. *Physica Scripta*. 2021; 96: 015216.
- [21] Abdelsalam SI, Mekheimer KS, Zaher AZ. Alterations in blood stream by electroosmotic forces of hybrid nanofluid through diseased artery: Aneurysmal/stenosed segment. *Chinese Journal of Physics*. 2020; 67: 314–329.
- [22] Akhtar S, McCash LB, Nadeem S, Saleem S, Issakhov A. Mechanics of non-Newtonian blood flow in an artery having multiple stenosis and electroosmotic effects. *Science Progress*. 2021; 104: 00368504211031693.
- [23] Akram J, Akbar NS, Tripathi D. Analysis of electroosmotic flow of silver-water nanofluid regulated by peristalsis using two different approaches for nanofluid. *Journal of Computational Science*. 2022; 62: 101696.
- [24] Khanduri U, Sharma BK, Sharma M, Mishra NK, Saleem N. Sensitivity analysis of electroosmotic magnetohydrodynamics fluid flow through the curved stenosis artery with thrombosis by response surface optimization. *Alexandria Engineering Journal*. 2023; 75: 1–27.
- [25] Manchi R, Ponalagusamy R. Pulsatile Flow of EMHD Micropolar Hybrid Nanofluid in a Porous Bifurcated Artery with an Overlapping Stenosis in the Presence of Body Acceleration and Joule Heating. *Brazilian Journal of Physics*. 2022; 52: 52.
- [26] Zaher AZ, Ali KK, Mekheimer KS. Electroosmosis forces EOF driven boundary layer flow for a non-Newtonian fluid with planktonic microorganism: Darcy Forchheimer model. *International Journal of Numerical Methods for Heat & Fluid Flow*. 2021; 31: 2534–2559.
- [27] Ellahi R, Rahman SU, Nadeem S, Akbar NS. Blood flow of nanofluid through an artery with composite stenosis and permeable walls. *Applied Nanoscience*. 2014; 4: 919–926.
- [28] Gandhi R, Sharma BK, Kumawat C, Bég OA. Modeling and analysis of magnetic hybrid nanoparticle (Au-Al₂O₃/blood) based drug delivery through a bell-shaped occluded artery with joule heating, viscous dissipation and variable viscosity effects. *Proceedings of the Institution of Mechanical Engineers, Part E: Journal of Process Mechanical Engineering*. 2022; 236: 2024–2043.
- [29] Basha HT, Rajagopal K, Ahammad NA, Sathish S, Gunakala SR. Finite Difference Computation of Au-Cu/Magneto-Bio-Hybrid Nanofluid Flow in an Inclined Uneven Stenosis Artery. *Complexity*. 2022; 2022: 1–18.
- [30] Gandhi R, Sharma BK. Modelling Pulsatile Blood Flow Using Casson Fluid Model Through an Overlapping Stenotic Artery with Au-Cu Hybrid Nanoparticles: Varying Viscosity Approach. In *International workshop of Mathematical Modelling, Applied Analysis and Computation* (pp. 155–176). Cham: Springer Nature Switzerland. 2022.
- [31] Kumawat C, Sharma BK, Muhammad T, Ali L. Computer simulation of two phase power-law nanofluid of blood flow through a curved overlapping stenosed artery with induced magnetic field: entropy generation optimization. *International Journal of Numerical Methods for Heat & Fluid Flow*. 2023.
- [32] Bhatti MM, Zeeshan A, Ellahi R. Simultaneous effects of coagulation and variable magnetic field on peristaltically induced motion of Jeffrey nanofluid containing gyrotactic microorganism. *Microvascular Research*. 2017; 110: 32–42.
- [33] Alharbi FM, Naeem M, Zubair M, Jawad M, Jan WU, Jan R. Bioconvection due to gyrotactic microorganisms in couple stress hybrid nanofluid laminar mixed convection incompressible flow with magnetic nanoparticles and chemical reaction as carrier for targeted drug delivery through porous stretching sheet. *Molecules*. 2021; 26: 3954.
- [34] Sharma BK, Khanduri U, Mishra NK, Chamkha AJ. Analysis of Arrhenius activation energy on magnetohydrodynamic gyrotactic microorganism flow through porous medium over an inclined stretching sheet with thermophoresis and Brownian motion. *Proceedings of the Institution of Mechanical Engineers, Part E: Journal of Process Mechanical Engineering*. 2023; 237: 1900–1914.
- [35] Mekheimer KS, Abo-Elkhair RE, Abdelsalam SI, Ali KK, Moawad AMA. Biomedical simulations of nanoparticles drug delivery to blood hemodynamics in diseased organs: Synovitis problem. *International Communications in Heat and Mass Transfer*. 2022; 130: 105756.
- [36] Mostapha DR, El-Dabe NTM. Peristaltic transfer of nanofluid with motile gyrotactic microorganisms with nonlinear thermic radiation. *Scientific Reports*. 2023; 13: 7054.
- [37] Khan NS. Bioconvection in second Grade Nanofluid Flow Containing Nanoparticles and Gyrotactic Microorganisms. *Brazilian Journal of Physics*. 2018; 48: 227–241.
- [38] Khan NS, Kumam P, Thounthong P. Renewable energy technology for the sustainable development of thermal system with entropy measures. *International Journal of Heat and Mass Transfer*. 2019; 145: 118713.
- [39] Ellahi R, Raza M, Vafai K. Series solutions of non-Newtonian nanofluids with Reynolds' model and Vogel's model by means of the homotopy analysis method. *Mathematical and Computer Modelling*. 2012; 55: 1876–1891.
- [40] Sharma BK, Khanduri U, Mishra NK, Mekheimer KS. Combined effect of thermophoresis and Brownian motion on MHD mixed convective flow over an inclined stretching surface with radiation and chemical reaction. *International Journal of Modern Physics B*. 2023; 37: 2350095.
- [41] Dubey A, Vasu B, Anwar Bég O, Gorla RSR, Kadir A. Computational fluid dynamic simulation of two-fluid non-Newtonian nanohemodynamics through a diseased artery with a stenosis and aneurysm. *Computer Methods in Biomechanics and Biomedical Engineering*. 2020; 23: 345–371.
- [42] Khanduri U, Sharma BK. Entropy analysis for MHD flow subject to temperature-dependent viscosity and thermal conductivity. In *Nonlinear Dynamics and Applications: Proceedings of the ICNDA 2022* (pp. 457–471). Cham: Springer International Publishing. 2022.
- [43] Gandhi R, Sharma BK, Khanduri U. Electromagnetohydrodynamics Casson pulsatile nanofluid flow through a bifurcated stenosed artery: Magnetically targeted drug delivery. *Journal of Applied Physics*. 2023; 134: 184701.
- [44] Vasu B, Dubey A, Bég OA, Gorla RSR. Micropolar pulsatile blood flow conveying nanoparticles in a stenotic tapered artery: NON-Newtonian pharmacodynamic simulation. *Computers in Biology and Medicine*. 2020; 126: 104025.
- [45] Jalili P, Sadeghi Ghahare A, Jalili B, Domiri Ganji D. Analytical and numerical investigation of thermal distribution for hybrid nanofluid

through an oblique artery with mild stenosis. SN Applied Sciences. 2023; 5: 95.

- [46] Tripathi J, Vasu B, Bég OA. Computational simulations of hybrid mediated nano- hemodynamics (Ag-Au/Blood) through an irregular symmetric stenosis. Computers in Biology and Medicine. 2021; 130: 104213.
- [47] Kumar Sharma B, Gandhi R. Entropy-driven optimization of radiative Jeffrey tetrahybrid nanofluid flow through a stenosed bifurcated artery with Hall effects. Physics of Fluids. 2023; 35: 121903.
- [48] Zhang B, Gu J, Qian M, Niu L, Zhou H, Ghista D. Correlation between quantitative analysis of wall shear stress and intima-media thickness in atherosclerosis development in carotid arteries. BioMedical Engineering OnLine. 2017; 16: 1–17.